Title

Spatiotemporal Variations of Evapotranspiration in Amazonia Using the Wavelet Phase Difference Analysis

Journal
Journal of Geophysical Research: Atmospheres, 127(10)

ISSN
2169-897X

Authors
Zhang, Juan
Feng, Ziyang
Niu, Jie
et al.

Publication Date
2022-05-27

DOI
10.1029/2021jd034959

Spatiotemporal variations of evapotranspiration in Amazonia using the wavelet phase difference analysis

Juan Zhang[1], Ziyang Feng[2], Jie Niu[2,3*], John M. Melack[4], Jin Zhang[2,3], Han Qiu[5], Bill X. Hu[3,6], and William J. Riley[7]

[1] College of Geographic and Environmental Science, Tianjin Normal University, Tianjin, 300387, China
[2]College of Life Science and Technology, Jinan University, Guangzhou 510632, China
[3]Green Development Institute of Zhaoqing, Zhaoqing, China
[4]Earth Research Institute, University of California, Santa Barbara, CA
[5]Joint Global Change Research Institute, Pacific Northwest National Lab, College Park, MD 20740, USA
[6]School of Water Conservancy and Environment, University of Jinan, Jinan 250022, China
[7]Earth Sciences Division, Lawrence Berkeley National Lab, Berkeley, CA

Correspondence to: J. Niu, jniu@jnu.edu.cn

Abstract

The relationships and seasonal-to-annual variations among evapotranspiration (*ET*), precipitation (*P*), terrestrial water storage anomalies (*TWSA*), radiation (downward shortwave radiation, *DSR*), and phenology (leaf area index, *LAI*) are complex across the Amazon basin. To analyze how *ET* is controlled by these influencing factors, we used wavelet phase difference (WPD) to investigate the effects of *P*, *TWSA*, *DSR*, and *LAI* on *ET* at different spatiotemporal scales. The Amazon-scale averaged *ET* has strong correlations with these factors at the annual and multi-year periodicities. The patterns of WPDs have south-north and west-east divides due to the significant variation in climatic conditions. The results demonstrate that *ET* is mainly affected by water and energy availability while vegetation regulates both processes. The deep soil moisture/groundwater can provide strong subsidies to *ET* during the meteorological dry season in the water-limited area of Amazon. The WPD can well reflect the responses of *ET* to the variations of *P*, *TWSA*, *DSR*, and *LAI*, and the process of vegetation sustaining *ET* in the dry years in the water-limited area of the Amazon.

1. Introduction

Evapotranspiration (*ET*) is an important part of the hydrological balance of the Amazon basin, as it links regional climate and forest function and plays a crucial role in the hydrological cycle. Large amounts of water are transferred from the land surface to the atmosphere via *ET* in the Amazon every day, which has a huge impact on the global energy budget (Bonan et al., 2018; Christoffersen et al., 2014; Hasler & Avissar, 2006; Restrepo-Coupe et al., 2016). Nonetheless, the spatiotemporal variation of *ET* across the Amazon basin, as well as the relative contributions of multiple drivers to this process, are still uncertain. Assessing the factors controlling *ET* in the Amazon basin, which largely depend on how tropical vegetation processes available energy and water, is still an essential research topic (Saleska et al., 2003; Swann et al., 2017).

The research on the seasonal variation of *ET* and its main controlling factors continued to be controversial since the early 1980s. Some models (Baker et al., 2008; Werth and Avissar, 2004) predicted water-limited *ET* seasonality that resembles precipitation (*P*) variations. This may be explained that increased atmospheric vapor pressure deficit (VPD) triggers the stomatal closure to avoid excess water loss in the dry season (Carnicer et al., 2013; Yuan et al., 2019). Gentine et al. (2012) concluded that the Amazon lies in a regime that is dominantly energy limited rather than water limited. Controls of *ET* across the Amazon basin vary. The evaluation of *ET* drivers in previous studies has not been conclusive in some cases, or only analyzed at the large scale for the whole Amazon basin. Malhi et al. (2002) measured the latent heat flux and analyzed its annual trend for the tropical rain forest close to Manaus, Brazil, pointing out that water limitation and stomatal control were the main factors driving seasonal *ET*. Recent studies based on eddy flux measurements indicate seasonal *ET* is driven by radiation, rather than water availability, in the Amazon (Juárez et al., 2007) and the tropics (Fisher et al., 2010), consistent with the greening of

Amazon forests during the dry season from satellite data (Brando et al., 2010; Doughty & Goulden, 2008; Saleska et al., 2007) and phenocam data (Gonçalves et al., 2020). Except for the satellite-based greenness, solar-induced chlorophyll fluorescence data from TROPOMI (Doughty et al., 2019) and GOME-2 (Doughty et al., 2020) can show the same effect as greenness during dry season for moist tropical forest. Maeda et al. (2017) suggested that both annual mean and seasonality of *ET* are driven by a combination of energy and water availability, as rainfall or radiation alone could not explain *ET* patterns. Therefore, more detailed studies are needed to explore the factor driving *ET*.

There are systematic biases of hydrologic and carbon fluxes and responses in Earth system models. For example, Tang et al. (2015) found that *ET* predicted using CLM4.5 at the Tapajos forest site in the Amazon basin compares poorly and is out of phase with MODIS data (MOD16A2). The modeling results from Verbeeck et al. (2011) showed that forests in some regions of the Amazon maintain high transpiration during the dry season. Due to the limited spatial coverage and the complex plant composition, the measurement of *ET* has great uncertainty (Culf et al., 2008). *ET* is a combined contribution of evaporation from the ground or other surfaces, as well as transpiration flux through plants, which reflects aspects of the plants' functioning. (Swann et al., 2017). Reduction in rainfall has diminished vegetation greenness in the tropical evergreen forest and subtropical grasslands, which coincides with the decline in terrestrial water storage (Hilker et al., 2014). This pattern is supported by severe drought suppressed photosynthesis (Doughty et al., 2015). The latest MOD16 global *ET* product agrees well with measurements from eddy flux towers (Mu et al., 2011), and shows higher *ET* in the dry season and lower *ET* in the wet season in the Amazonian tropics. Groundwater storage has a strong influence on atmospheric and terrestrial hydrological processes by affecting soil moisture and *ET* rate in the Amazon (Lin et al., 2016). Several modeling studies have also concluded that surface runoff is rare and groundwater plays a key role in Amazon hydrology (Miguez-Macho & Fan, 2012a), and groundwater has a significant influence on soil moisture and *ET* (Miguez-Macho & Fan, 2012b). Our recent analysis with a three-dimensional hydrologic model applied to an Amazon watershed (Niu et al., 2017) demonstrated that lateral fluxes, especially groundwater flows, have a large impact on subsurface hydrologic processes.

The estimation technology of the phase difference has gone deep into many fields, such as biomedicine, ultrasound, radar, and sonar (Etter and Stearns, 1981; Carter, 1993). It has an important significance to accurately estimate the transmission delay between two signals. Although many methods are used to calculate the phase difference between two signals (Micheletti, 1991; Audoin and Roux, 1996; Maskell and Woods, 2002; So, 2006; Bjorklund and Ljung, 2009), none of them can better deal with the problem of phase mutation like the wavelet transform. Compared with the traditional estimations of the phase difference, wavelet transform also improves the accuracy of estimation. Wavelet analysis has been applied widely in previous studies to identify the annual periodicity of the hydrologic and climate fluxes and detect their long-term trends (Andreo et al., 2006); to detect potential flood triggering conditions (Schaefli et al., 2007); and to extract significant information and the characteristic time scale of the dominant hydrologic processes (Zhang et al., 2017). The method has also been applied to monthly discharges of Amazon River to advise physical explanations for time-scale dependent relationships (Labat et al., 2005). To the best of our knowledge, due to the scarcity of observations, no previous studies using wavelet power spectral has analyzed the relationships between *P* or terrestrial water storage anomalies (*TWSA*), and *ET* in the Amazon. Moreover, the application of the wavelet phase difference (WPD) in the Amazon basin and focusing on the phase lags of *ET-P* and *ET-TWSA* are relatively rare. In order to accurately identify the time-delay characteristics at the specified frequency and phase mutation of hydrological components, it is necessary to explore the application prospect of WPD in the hydrological cycle.

The Budyko curve framework is a classic empirical approach to analyze annual hydrological budgets and the inter-annual variability of annual hydrological budgets (Bukydo, 1974) and annual water balances (Yang et al., 2007; Wang, 2012). A recent study found that the errors between observations and the traditional Budyko curve could be reduced if the equation was corrected using information extracted from the Gravity Recovery and Climate Experiment (GRACE) *TWSA* (Fang et al., 2016). Using the Budyko framework is conducive to understand the energy-limited and water-limited regimes across the Amazon basin.

In this study, by analyzing the WPDs between *P*, *TWSA*, downward shortwave radiation (*DSR*), or leaf area index (*LAI*), and *ET*, we can explore the interaction between rainfall, terrestrial water storage, radiation or phenology, and *ET* flux at three spatial resolutions (whole Amazon basin, the individual grid cells, and four zones), including the effect of the drought events, especially in years 2005 and 2010 when droughts over Amazonia were very strong, which is referred to as a once-in-a-century drought (Liu et al., 2018). The purpose is to dynamically analyze the main factors controlling *ET* across the Amazon basin and promote the potential application of WPD in hydrology. We also apply the Budyko framework to evaluate the annual hydrological budgets in different sub-basins of the Amazon. With these tools we address the following questions: (1) How is *ET* affected by rainfall, terrestrial water storage, radiation, and phenology in the Amazon basin at different temporal and spatial scales? (2) What is the difference in the impact of terrestrial water storage on *ET* between the wet and dry years? And (3)

Can the WPD analysis reflect the dynamic lag relationship between *ET* and influencing factors, as well as the process of water supply?

2. Methods

2.1 Data Sources

The Tropical Rainfall Measuring Mission (TRMM, available from NASA, (http://trmm.gsfc.nasa.gov/) 3B42 V7 daily data with 0.25-degree spatial resolution were used for *P*. *ET* was derived from Moderate Resolution Imaging Spectroradiometer (MODIS) global terrestrial *ET* (MOD16A2) product at 1 km resolution (http://www.ntsg.umt.edu/project/mod16) from 2002 to 2013, which used a modified Penman-Monteith method (Mu et al., 2011). It separated the dry canopy surface from the wet. Therefore, *ET* is the sum of water lost to the atmosphere from soil surface evaporation, canopy evaporation from the water intercepted by the canopy, and transpiration from plant tissues. This product agrees well with measurements from 46 eddy flux towers, including two towers in the Amazon basin. Different estimation methods of *ET* had been proposed in some recent studies (Paca et al., 2019; Swann et al., 2017; Wu et al., 2020; Xu et al., 2019), and these products were compared with MOD16A2 in the meantime. Compared with these studies, although MOD16A2 tends to underestimate lower values of *ET* and overestimate the higher values, the long-term annual *ET* is consistent among these estimates, which has little effect on the study of the phase difference. The most recent release of the spherical harmonics GRACE observations was used to estimate terrestrial water storage anomalies (*TWSA*), which includes the variations of groundwater, soil moisture, surface water, vegetation water, snow, and ice. *TWSA* (RL05) was provided by the Tellus product processed by the Jet Propulsion Laboratory (available at http://grace.jpl.nasa.gov/). This distributed GRACE product has been “destriped” and smoothed using a 300 km wide Gaussian filter to minimize north-south stripes, and is appropriate for land hydrology applications (Landerer & Swenson, 2012; Swenson & Wahr, 2006). The resolution for *TWSA* dataset is monthly temporally and 1-degree spatially. Optical satellite vegetation data were used to characterize canopy dynamics, which includes *LAI*. *LAI* is defined as the one-sided green leaf area per unit ground area in broadleaf canopies, and one-half of the total needle surface area per unit ground area in coniferous canopies. The *LAI* product (MCD15A2H) used is the latest version (Collection 6) of MODIS from Terra and Aqua combined (Yan et al., 2016), which provides an 8-day composite dataset with a 500-meter resolution.

Land cover information was obtained from the Collection 6 MODIS Terra land cover dynamics product (MCD12Q2) that mapped global land surface phenology metrics at 500-meter spatial resolution and annual time step. Phenology metrics were derived from the time series of MODIS observed land surface greenness. The integrated time series of the 2-band Enhanced Vegetation Index calculated from MODIS nadir BRDF adjusted surface reflectance (NBAR-EVI2) over a vegetation cycle was used to analyze in this study. The MODIS Terra and Aqua combined Level 3 product (MCD18A1 Version 6.1) generated 3-hourly Downward Shortwave Radiation (*DSR*) gridded data. *DSR* is incident solar radiation over land surfaces in the shortwave spectrum (300-4000 nanometers).

The sub-basin delineation map applied here was obtained from a topography-independent analysis method (Mayorga et al., 2005) using the vector river network from the Digital Chart of the World (DCW, Danko, 1992). The map includes the sub-basin boundaries of the major tributaries to the main stem of the Amazon River (http://daac.ornl.gov/LBA/guides/CD06_CAMREX.html)

2.2 Wavelet Analysis

Although the Fourier transform can process the signal into the frequency domain for analysis, it can only analyze the time series from the frequency domain alone. The wavelet transform can reflect the localized characteristics of the signal in both the time domain and the frequency domain, which overcomes the limitations of the traditional Fourier transform. Briefly, similar to Fourier analysis, wavelet analysis extracts frequency information (called scales) from time series. Wavelet analysis also reveals the timing of the features. For this work, we adopted the algorithm of wavelet transform from Torrence and Compo (1998). The wavelet transform decomposes the signal into a series of wavelet functions, generated by the mother wavelet function. Each wavelet is derived from a mother wavelet $\psi(t)$ by expansion and translation to yield $\psi_{a,b}(t)$:

$$\psi_{a,b}(t) = \frac{1}{\sqrt{a}}\psi\left(\frac{t-b}{a}\right), a, b \in R \qquad (1)$$

where a is the frequency parameter, and b is the time parameter. In general, the complex non-orthogonal Morlet wavelet function is used as the mother wavelet function, which is defined as ψ_0. For time series $x(t)$ if we denote its continuous wavelet transform as $W_x(a,b)$:

$$W_x(a,b) = \frac{1}{\sqrt{a}}\int_{-\infty}^{+\infty} x(t)\psi_0^*\left(\frac{t-b}{a}\right)dt \qquad (2)$$

where * denotes the conjugate complex value. Then the wavelet power spectrum is defined as $|W_x(a,b)|^2$, and the instantaneous phase of time series $x(t)$ is $atan2\left(\frac{Imag\{W_x(a,b)\}}{Real\{W_x(a,b)\}}\right)$. *atan2* is the four-quadrant inverse tangent function with the value range of $[-\pi, \pi]$. $Real\{W_x(a,b)\}$ and $Imag\{W_x(a,b)\}$ denote the real and imaginary parts of the continuous wavelet transform $W_x(a,b)$, respectively. The $|W_x(a,b)|^2$ provides insight into the temporal-scale variability of the time series.

The global wavelet power spectrum is defined as the time-averaged wavelet spectrum over all the local wavelet spectra:

$$\overline{\boldsymbol{W}}_{\boldsymbol{x}}{}^{\boldsymbol{2}}(\boldsymbol{a}) = \frac{\boldsymbol{1}}{\boldsymbol{n}}\sum_{\boldsymbol{b}=\boldsymbol{1}}^{\boldsymbol{n}} |\boldsymbol{W}_{\boldsymbol{x}}(\boldsymbol{a},\boldsymbol{b})|^{\boldsymbol{2}} \tag{3}$$

where n is the number of points in the time series.

Given two time series $x(t)$ and $y(t)$, with wavelet transforms $W_x(a,b)$ and $W_y(a,b)$, the cross-wavelet spectrum is defined as:

$$\boldsymbol{W}_{\boldsymbol{xy}}(\boldsymbol{a},\boldsymbol{b}) = \boldsymbol{W}_{\boldsymbol{x}}(\boldsymbol{a},\boldsymbol{b})\boldsymbol{W}_{\boldsymbol{y}}^{*}(\boldsymbol{a},\boldsymbol{b}) \tag{4}$$

where $\boldsymbol{W}_{\boldsymbol{y}}^{*}(\boldsymbol{a},\boldsymbol{b})$ is the complex conjugate of $W_y(a,b)$. The cross-wavelet power is $\left|W_{xy}(a,b)\right|$, and indicates local covariance between the time series at each predefined scale, revealing the magnitude of influence between two time series on a given temporal scale, which includes both positive and negative correlation. Since time series have finite length, the wavelet transform will not be completely localized, meaning there are edge effects in the time dimension. Therefore, the cone of influence (COI) is used for wavelet analysis (Torrence and Compo, 1998).

As wavelet transforms can be robust tools for handling the localized characteristics between signals in the time-frequency domain, WPD shows its advantages in non-stationary time series. WPD of the two signals is computed as $atan2\left(\frac{Imag\{W_{xy}(a,b)\}}{Real\{W_{xy}(a,b)\}}\right)$ with the value range of [$-\pi$, π]. The phase difference is used for two time series with the same frequency. According to the cross-wavelet spectrum analysis, the strong resonance of the periodicity between $x(t)$ and $y(t)$ is mainly explored in this study. In other words, we focus on the difference in timing between two time series at their high-power spectrum. In order to show WPD (ϕ) more intuitively, we multiplied the coherence phase in proportion to 2π by their coherent period at their strong cross-wavelet power spectrum band:

$$\boldsymbol{\phi = atan2(\frac{Imag\{W_{xy}(S_{scale}\}}{Real\{W_{xy}(S_{scale})\}}) \cdot \frac{S_{scale}}{2\pi}} \quad (5)$$

where S_{scale} means the time scale (or period) of the cross-wavelet power spectrum band, which does not change over time. The range of the WPD is constrained at $[-\frac{S_{scale}}{2}, \frac{S_{scale}}{2}]$. When $\phi = 0$, it means that the variations of two time series $x(t)$ and $y(t)$ over time are in phase at the specified frequency (S_{scale}), while the WPD of $\mp\frac{S_{scale}}{2}$ indicates an anti-phase relation between $x(t)$ and $y(t)$. For $|W_{xy}(a,b)|^2$, if $\phi > 0$, it represents that $x(t)$ leads $y(t)$. If $\phi < 0$, it denotes that $x(t)$ lags behind $y(t)$., The leading and lag relationship between $x(t)$ and $y(t)$ cannot be distinguished when ϕ is close to $\mp\frac{S_{max}}{2}$, while it can be determined when ϕ is close to 0. In theory, the range of the phase difference also can be added or minus N periods, where N is an integer. Therefore, the magnitude of the WPD needs to be determined in combination with specific research problems. Although the WPD has been defined when the cross-wavelet analysis method was developed, there are few studies on its application to the best of the authors' knowledge. The WPD is used to analyze the time lag relationships between hydrological components at each defined scale, providing very useful information on certain physical phenomena. This study also widens its application field.

We calculated the WPDs between *P*, *TWSA*, *DSR* or *LAI*, and *ET* for three spatial resolutions: (1) averaged across the Amazon basin, (2) for individual 1-degree grid cells, and (3) averaged for four zones in the Amazon basin based on the WPDs at the 1-degree resolution. The underlying resolutions of *P*, *ET*, *TWSA*, *DSR*, and *LAI* are 0.25-degree, 1 km, 1-degree, 1 km, and 500 m respectively as described in Section 2.1. Since this study focused on the regional scale, *P*, *ET*, *DSR*, and *LAI* were converted to the same 1-degree resolution as *TWSA* by the moving average technique to calculate WPDs at 1-degree. Comparisons among these spatial averaging units allow us to analyze the behavior of the coherences at different spatial scales. Hereafter, we define the WPDs between *ET* and *P* at the different spatial scales as ϕ_{ET-P}^{Amazon}, $\phi_{ET-P}^{1-degree}$, and ϕ_{ET-P}^{Zone}, the WPDs between *ET* and *TWSA* as $\phi_{ET-TWSA}^{Amazon}$, $\phi_{ET-TWSA}^{1-degree}$, and $\phi_{ET-TWSA}^{Zone}$, the WPDs between *ET* and *DSR* as ϕ_{ET-DSR}^{Amazon}, $\phi_{ET-DSR}^{1-degree}$, and ϕ_{ET-DSR}^{Zone}, and the WPDs between *ET* and *LAI* as ϕ_{ET-LAI}^{Amazon}, $\phi_{ET-LAI}^{1-degree}$, and ϕ_{ET-LAI}^{Zone} for the whole Amazon basin, the individual grid cells, and four zones, respectively. A positive ϕ_{ET-P}^{Amazon} would mean that *ET* signal leads that of *P*.

For simplicity and convenience, the time scales and wavelet power spectrum are presented using the 2-based logarithmic scale in all figures shown in the results sections below.

2.3 Budyko framework

The Budyko hypothesis assumes that the long-term (2002 - 2013) partitioning of *P* into *ET* and runoff can be determined from available water measured as precipitation and available energy measured as potential evapotranspiration (E_P). Based on the Budyko hypothesis, the ratio between actual evapotranspiration (E_A) and *P* is related to the aridity index (the ratio between E_P and *P*, $\frac{E_P}{P}$), or the climate dryness index (Budyko, 1974):

$$\frac{E_A}{P} = \left\{\frac{E_P}{P} \tanh\left(\frac{E_P}{P}\right)\left[1 - \cosh\left(\frac{P}{E_P}\right) + \sinh\left(\frac{P}{E_P}\right)\right]\right\}^{0.5} \tag{6}$$

3. Results and Discussion

3.1 Wavelet analysis for Amazon-scale averaged variables

The wavelet power spectra of spatially averaged *P*, *ET*, *TWSA*, *DSR*, and *LAI* data over the whole Amazon basin reveal, for each dataset, a band of maximum power across all years with approximately a 12-month period (Figure 1(a), (b), (c), (d), and (e)). For *ET* the 95% confidence contour band ends around 2010, as there is a substantial change in the *ET* cycle after 2010. The pattern of a discontinuous maximum power spectrum band for *ET* can be explained by the drought event in 2010 and its monthly time series with more frequent fluctuations after 2010 than before (Figure 3(b)). Meanwhile, the global wavelet power spectra identify the main fluctuations of the time series (Figure 1(f), (g), (h), (i), and (j)). As expected, the wavelet analysis captured the annual cycles of the three hydrological fluxes. Additionally, *ET* also shows a smaller 3 – 6 months peak, as well as a 2 – 4 years peak (Figure 1(g)). Larger coherence indicates stronger linear correlation between two time series at the given time scale. Patches of high coherence around 1-year periodicity between *ET* and *P*, between *ET* and *TWSA*, between *ET* and *DSR*, and between *ET* and *LAI* are evident (Figure 2). It can be indicated that *ET* has a strong resonant periodicity with *P*, *TWSA*, *DSR*, and *LAI* at the annual scale, however, the covariation weakens substantially there since the annual cycle in *ET* has been interrupted after 2010 (Figure 1(b)). Between ~2006 and ~2010, the high coherence at a 2 – 4 years period (Figure 2(a), (b), and (d)) corresponds to the 2 – 4 years fluctuation in the *ET* wavelet spectrum (Figure 1(g)).

In order to obtain the anomalies in *ET* responding to anomalies in other influencing factors more clearly, the seasonality of original datasets was adjusted to further analyze their correlations. The results of the seasonality adjusted wavelet analysis are listed in Figures S1 and S2. *P*, *DSR*, and *LAI* have significant and discontinuous high-power regions at 2 – 6 months period (Figure S1(a), (d), and (e)), while *P*, *ET*, and *TWSA* have significantly high-power bands at the 1-year periodicity from 2003 to 2005 (Figure S1(a), (b), and (c)). The strong resonance at multi-year (2 – 4 years) periodicities between *ET* and *P*, between *ET* and *TWSA*, and between *ET* and *LAI* are evident (Figure S2(a), (b), and (d)), while the strong resonances at the 1-year periodicity between *P* / *TWSA* / *DSR* / *LAI* and *ET* are significant and discontinuous. These possibly relate to long-term climatic drivers (e.g., El Niño with ~3 – ~7 years periodicity) or the tropical Atlantic and Pacific Sea surface anomalies (~2 – ~6 years periodicity) (Fassoni-Andrade et al., 2021). Their discontinuous resonances at intra-annual periods correspond to the significant high-power regions at 2 – 6 months period (Figure S1). ET is severely affected in the rainiest months (La Niña phenomena during 2007 – 2008 and 2011 – 2012), and the least rainy months (El Niño phenomena during 2002 – 2005 and 2009 – 2010) (Moura et al., 2019).

3.2 Phase difference for Amazon-scale averaged variables

The WPD between *ET* and *P* reflects the time lag relationship between *ET* and *P*. For instance, if rainfall would quickly become *ET*, we expect to see a ϕ_{ET-P}^{Amazon} of ~0. However, as the leaves of tropical forests flush and grow at the beginning of the dry season when precipitation decreases and radiation increases, we must also consider the time it takes for growing. Hence, we can expect a small negative ϕ_{ET-P}^{Amazon}, meaning that *ET* occurs after *P*. It indicates that *ET* lags behind *P* due to the period required for growth and the period with cloud-cover (the decrease in energy availability caused by increased cloudiness during the wet regions/seasons). While, a positive ϕ_{ET-P}^{Amazon} (*ET* signal leads that of *P*, which means that *ET* occurs before *P*) is quite intriguing and could possibly suggest that the cloud-suppressed (radiation-limited) forest has adapted to and anticipated the coming dry season and increases leaf allocation toward the end of the rainy season, as suggested by Fu and Li (2004), or it may be that photosynthesis and transpiration of evergreen plants increase during the dry season in the moist tropical Amazon (Saleska et al., 2007; Doughty et al., 2019; Doughty et al., 2020).

Since the WPD is significant only at the continuous and strong resonance period, the subsequent results of WPDs are only valid for the the original dataset at 1-year time scale. The averaged WPDs across the Amazon basin scale, ϕ_{ET-P}^{Amazon}, $\phi_{ET-TWSA}^{Amazon}$, ϕ_{ET-DSR}^{Amazon}, and ϕ_{ET-LAI}^{Amazon} are presented in the Figure 3(a). For the Amazon basin, ϕ_{ET-P}^{Amazon} ranges from ~2 to ~4 months, $\phi_{ET-TWSA}^{Amazon}$ ranges from ~3 to ~8 months, ϕ_{ET-DSR}^{Amazon} ranges from -4 to -2 months, and ϕ_{ET-LAI}^{Amazon}

ranges from -5 to -2 months. It can be seen that *ET* occurs after *LAI* and *DSR*, while before *P* and *TWSA*. The peak of *ET* appears at the beginning of wet season (Figure 3 (b)). The severe meteorological drought in 2005 and 2010 both began in the wet season and ended right before the end of the wet season. Seasonal cycles of *P*, *TWSA*, *DSR*, and *ET* over the whole Amazon are showed in Figure S3. The response of soil moisture lags rainfall for days to 1-month (Figure S3 (a)), as soil acts as a temporary reservoir to accumulate rainfall (Liu et al., 2014). WPDs of ϕ_{ET-P}^{Amazon} and $\phi_{ET-TWSA}^{Amazon}$ decreased slightly in 2005 and 2010, meaning the degrees of resonance between *P* or *TWSA*, and *ET* are enhanced in drought event. Moreover, the two WPDs are qualitatively correlated in time, except for 2010, when a severe drought occurred from August to October. Both ϕ_{ET-P}^{Amazon} and $\phi_{ET-TWSA}^{Amazon}$ decreased comparing to those in 2009, but after 2010, $\phi_{ET-TWSA}^{Amazon}$ increased from ~ 5 months to more than 7 months while ϕ_{ET-P}^{Amazon} remained relatively constant at ~4 months (Figure 3(a)). It could suggest a pattern that *ET* will increase even when there is insufficient rainfall. The deep soil water/groundwater reserves are still maintained at a high level to provide sufficient water for *ET* during the meteorological dry season. Miguez-Macho and Fan (2021) found that 70% of plant transpiration relies on *P* in the current month, 18% relies on past *P* stored in deeper unsaturated soils and/or rocks, only 1% relies on past *P* stored in groundwater, and 10% relies on groundwater from *P* fallen on uplands via river-groundwater convergence toward lowlands. Therefore, the process of *ET* affected by rainfall and deep soil moisture/groundwater has been changed by the drought event. ϕ_{ET-LAI}^{Amazon} and ϕ_{ET-DSR}^{Amazon} increased in 2005 and 2010, indicating that *ET* may be delayed due to the reduction of rainfall.

To further analyze the spatiotemporal distribution of WPDs and the lag relationships between *ET* and other climatic indicators, the 1-degree and four-zones WPDs within the Amazon basin are examined in the following sections.

3.3 Phase difference for 1-degree spatial scale variables

The 1-degree spatial scale WPDs of $\phi_{ET-P}^{1-degree}$, $\phi_{ET-TWSA}^{1-degree}$, $\phi_{ET-DSR}^{1-degree}$, and $\phi_{ET-LAI}^{1-degree}$ are presented in Figures 4 – 7, respectively. Large south-to-north and small west-to-east gradients occur for WPDs across all years analyzed (Figures 4 – 7), especially the WPD between *ET* and *P*. The small and negative values of $\phi_{ET-P}^{1-degree}$ and $\phi_{ET-TWSA}^{1-degree}$ are distributed in the north of the Amazon basin, where there is sufficient rainfall. According to the sufficient precipitation and low radiation in this area, the WPD is described as *ET* lags behind *P* and *TWSA* (Figures 4 – 5), and *ET* leads to *DSR* (Figure 6). It possibly indicates that cloudy conditions limit the available energy driving *ET* (Zhang et al., 2001). To further distinguish the different water-limited and energy-limited regions, 33 sub-basins within the Amazon basin are examined by using the Budyko analysis (Figure 8). Sub-basin #1 is narrow, crosses almost the entire Amazon basin horizontally, and closely conforms to the Amazon River (cross hatched in Figure S4). The sub-basin delineation from Mayorga et al. (2005) is not accurate for sub-basin #1 since it only approximates the floodplain of the main stem of the Amazon River and includes minor catchments bordering the floodplain. Thus, the results for this sub-basin #1 will not be discussed. Based on the result of the Budyko analysis, the sub-basins located in the north of the Amazon basin are energy limited (Figure 8). For these sub-basins, *ET* may be suppressed by excessive rainfall and low radiation. Excessive rainfall suppresses the respiration of root cells, which makes the plants come into a state of water shortage. The stomata of plants are closed, which affects their transpiration. The area where the absolute values of $\phi_{ET-P}^{1-degree}$ and $\phi_{ET-TWSA}^{1-degree}$ are close to 6 months is located in the central of the Amazon basin (Figures 4 – 5), suggesting that the relationship of the time lag between *P* or *TWSA*, and *ET* in this area is not clear. $\phi_{ET-DSR}^{1-degree}$

and $\phi_{ET-LAI}^{1-degree}$ are close to 0 month in this area. The strong resonances indicate that *DSR* and *LAI* jointly affect *ET* in the central of the Amazon basin.

The small and positive $\phi_{ET-P}^{1-degree}$ is distributed in the southwest of the Amazon basin, meaning that *ET* leads to *P*. The $\phi_{ET-DSR}^{1-degree}$ in this area cannot be guaranteed which time series is lagged. Sub-basin #33 is water-limited and energy-limited (Figure 8), which is located southwest of the Amazon basin. All sub-basins (#5, #9, #16) located in the southeast of the Amazon basin are generally water-limited compared to other sub-basins (Figure 8). $\phi_{ET-P}^{1-degree}$ and $\phi_{ET-TWSA}^{1-degree}$ are closed to zero in the southeast of the Amazon basin (Figures 4 – 5), suggesting that *P* lags slightly behind *ET*. The mean annual precipitation (MAP) of this area corresponds to the threshold for light/water limitation (2000mm MAP) mentioned in many previous studies (Doughty et al., 2019; Doughty et al., 2020; Wagner et al., 2016). The importance of plant control should be considered in the water balance accounting of the water-limited area. The *ET* rate can increase even in rainfall deficit conditions, which can be explained by plants access to deep soil water (Maeda et al., 2017). Vegetation in the southern Amazon is particularly sensitive to changes in the length of the dry season. It is widely affected by anthropogenic forcing, especially along the “Arc of Deforestation” around the southeast edge of the forest (Wongchuig et al., 2021). Therefore, $\phi_{ET-LAI}^{1-degree}$ in the southern Amazon are complex, which may be caused by the anthropogenic activities in areas like pasture, agriculture, and deforested area.

In addition, the $\phi_{ET-P}^{1-degree}$ and $\phi_{ET-TWSA}^{1-degree}$ close to zero in the southeast of the Amazon basin vary to the larger WPD across years, meaning that the lag time between *P* or *TWSA*, and *ET* has increased. The increase of WPDs may be accompanied by deforestation, large rainfall, or reduced radiation, which may affect lag relationships between *ET* and other factors (*P*, *TWSA*, *DSR*, and *LAI*). It possibly indicates that the vegetation area in this area is reduced due to deforestation activities, fire, logging, or extreme drought events (Spracklen et al., 2012; Brando et al., 2014; Brown and Brown, 2016; Qin et al., 2017). Based on the land cover dynamics (MCD12Q2) for 2005, 2010, 2011, and 2013 (Figure S5), the value of NBAR-EVI2 in the southern Amazon basin is relatively large, corresponding to the area of WPDs changed. The WPD of $\phi_{ET-TWSA}^{1-degree}$ has zero-to-positive variation patterns from 2002 to 2013 (Figure 5), suggesting that the decrease in *ET* after forest deforestation or degradation (Brown and Brown, 2016; De Oliverira et al., 2018; Staal et al., 2020) was firstly caused by a reduction of the capacity of the vegetation to access subsurface water (Zemp et al., 2017; Aparecide et al., 2020). Humphrey et al. (2018) proved that the inter-annual variability of the CO_2 growth rate is closely related to that of *TWSA*. Considering that interannual fluctuation in *TWSA* strongly affects the terrestrial carbon sink and the importance of the interactions between the water and carbon cycles, the variability of *ET* is also closely associated with *TWSA*. $\phi_{ET-P}^{1-degree}$ has zero-to-positive variation patterns (Figure 4), which indicates that the interaction between *ET* and *P* has changed in the south of Amazon region due to deforestation and degradation.

To further distinguish the relationship between *P* or *TWSA*, and *ET* in difference regions, the WPDs ϕ_{ET-P}^{subbas} and $\phi_{ET-TWSA}^{subbas}$ of 33 sub-basins within the Amazon basin are examined (Figure S4). Inter-annual variability in ϕ_{ET-P}^{subbas} (blue lines) and $\phi_{ET-TWSA}^{subbas}$ (red lines) differs among the sub-basins, although coherent patterns are evident. The linear correlations between ϕ_{ET-P}^{subbas} and $\phi_{ET-TWSA}^{subbas}$ are higher and more significant in the southern basins (#5, #9, #16, #20, #25, #32 and #33) than those of other basins. These indicate that rainfall and water storage have mutual constraints in affecting *ET*. Qualitatively, north-to-south pattern of WPDs are obvious due to these sub-basins vary considerably in topography and rainfall patterns. For these southern basins, the linear correlations between ϕ_{ET-P}^{subbas} and $\phi_{ET-TWSA}^{subbas}$ are more statistically significant, indicating that if the immediate supply from P is insufficient to maintain ET, deep soil moisture/groundwater plays an important role.

3.4 Phase difference for four zones' averaged variables

According to the patterns of WPDs from Section 3.3, there are spatially varying differences in the interaction mechanism of *P*, *TWSA*, *DSR* or *LAI*, and *ET*. Therefore, the Amazon basin was divided into four zones on the basis of WPDs at the 1-degree spatial scale (see Text S1 and Figure S6).

Both WPDs of $\phi_{ET-P}^{Zone\,1}$ and $\phi_{ET-TWSA}^{Zone\,1}$ are negative from 2002 to 2012 (Figure 9(a)), indicating that *ET* lags behind *P* and *TWSA* (*ET* occurs after *P* and *TWSA*). Meanwhile, $\phi_{ET-DSR}^{Zone\,1}$ and $\phi_{ET-LAI}^{Zone\,1}$ are positive (*ET* occurs before *DSR* and *LAI*), especially $\phi_{ET-LAI}^{Zone\,1}$ remains around 1 month. The small $\phi_{ET-LAI}^{Zone\,1}$ means that the growth of vegetation is closely related to ET. The annual *P* in this zone is larger than those in other zones (Figures 9(c), 10(c), 11(c), and 12(c)), which implies that this zone should not be water-limited. The suppression of ET in Zone 1 is most likely that the sufficient *P* and cloud-cover limit the energy available to drive ET. Seasonal cycles of *P*, *TWSA*, *DSR*, and *ET* in different zones are showed in Figures S7 – S10. The peak of *ET* occurs 2 months after the heavy rainfall, as well as 1 – 2 months before the arrival of the dry season in Zone 1 (Figures S7 – S9). Meanwhile, *TWSA* responds quickly to *P* (Figure S7). Except for $\phi_{ET-LAI}^{Zone\,1}$, other WPDs change significantly during drought events. These may indicate that the reduction of humidity and the elevation of temperature cause the increase of ET rate in less rainy months in Zone 1. Meanwhile, less severe droughts for the northern Amazon may enhance vegetation growth due to increased solar radiation.

Zone 2 covers in the central of the Amazon basin. Both WPDs of $\phi_{ET-P}^{Zone\,2}$ and $\phi_{ET-TWSA}^{Zone\,2}$ range from ~-4 months to ~-6 months from 2002 to 2013 (Figure 10(a)). Thus, it means that the lag relationship between P or $TWSA$, and ET may not be accurately determined in Zone 2. The peak of ET occurs at the end of the wet season, and the peak of $TWSA$ occurs 1 month after the heavy rainfall (Figures S7 and S9). However, both WPDs of $\phi_{ET-DSR}^{Zone\,2}$ and $\phi_{ET-LAI}^{Zone\,2}$ are close to zero, indicating the strong degrees of resonances between DSR or LAI, and ET. All WPDs are slightly decreased during the drought events, which indicate that the degrees of resonance between P, $TWSA$, DSR or LAI, and ET have enhanced during drought events. Due to the fewer anthropic pressures and the denser vegetation cover, the higher incidence of solar radiation increases vegetation transpiration and ET from water bodies, which regulates the increase of ET (Flantua et al., 2015). The peak of ET occurs after the wet season when radiation begins to enhance to provide energy for ET in Zone 1 and Zone 2.

Zone 3 contains the Peruvian region and the Andes on the southwest edge of the Amazon basin, where both $\phi_{ET-P}^{Zone\,3}$ and $\phi_{ET-TWSA}^{Zone\,3}$ remained positive from 2002 to 2013 (Figure 11(a)). ET leads that of P and $TWSA$, and the lag relation between LAI and ET cannot be determined in Zone 3. The peak of ET occurs 1 – 2 months before the heavy rainfall, and 2 – 4 months after the dry season (Figure 11(b)). And the peak of $TWSA$ occurs in the middle of wet season (Figure S7). $\phi_{ET-P}^{Zone\,3}$ and $\phi_{ET-TWSA}^{Zone\,3}$ have decreased in drought events, which promote the response of ET to P and $TWSA$. $\phi_{ET-DSR}^{Zone\,3}$ increases in drought events indicates that ET begins to be limited by available water with the increase of radiation.

The smaller WPDs of $\phi_{ET-P}^{Zone\,4}$ and $\phi_{ET-TWSA}^{Zone\,4}$ (Figure 12(a)) indicate that the degrees of resonance between P or $TWSA$, and ET for Zone 4 are stronger than others, while the peak of ET occurs in the middle of the wet season (Figure 12(b)), and the trough of ET occurs when the drought is most severe in the dry season (Figures S8 – S9). The variations of WPDs for Zone 4 averaged variables correspond well to the drought events. The degrees of resonance between P, *TWSA* or *LAI*, and *ET* have slightly enhanced in droughts, indicating that drought events can affect the water supply mechanism of *ET*. This is the regime with a higher aridity index and more deforestation activities, where may occur water-limited in some years (Figure 8). Due to the interaction between vegetation and atmosphere, deforestation in the Amazon basin is expected to exacerbate the dry season and inter-annual drought (Medvigy et al., 2011; Spracklen et al., 2012). The close response of $\phi_{ET-P}^{Zone\,4}$ to the variation of the annual *P* supports the hypothesis that *P* relies on rapid evaporation when it is small. Two WPDs of $\phi_{ET-P}^{Zone\,4}$ and $\phi_{ET-TWSA}^{Zone\,4}$ are qualitatively correlated in time, except for the drought event in 2010. The large variation and the small WPD of $\phi_{ET-TWSA}^{Zone\,4}$ in 2010 indicate that groundwater or soil moisture supports *ET* during the dry periods via water supply mechanism (rooting depth and interaction between groundwater and soil) and vegetation water requirement (Christoffersen et al., 2014). However, the plant roots in deforested and grassland areas in this region are shallow, so their access is limited to the water available in the upper soil layer. By contrast, forest trees can obtain groundwater in the deeper soil areas, maintaining an optimum water balance and avoiding a decrease in *ET* in the drier months or even resulting in an increase in *ET* during this period due to ideal atmospheric conditions.

The correlation between *P* or *TWSA*, and *ET* across the different area of the Amazon basin vary. Evaporation demand (especially net radiation) plays a more important role in wetter forests, and deep soil moisture (or *P*) has larger effects in the relative drier area (da Rocha et al., 2009). In the southern of Amazon basin, the soil water storage still remains relatively large after the start of the dry season (i.e., when rainfall is small). Along with the cumulative water deficit increases, the soils reach their lower water storage capacity, which can be regarded as temporary water restrictions. Then 3 months after the peak of the dry season, the rainy season has already started to provide enough water for evergreen plants. Therefore, the annual flux of *ET* remains relatively stable in dry years.

4. Conclusions

Using wavelet transform and wavelet phase difference (WPD) analysis, we found that Amazon-scale averaged evapotranspiration (*ET*) has strong correlations with precipitation (*P*), the terrestrial water storage anomalies (*TWSA*), downward shortwave radiation (*DSR*), and leaf area index (*LAI*) at the annual and multi-year periodicities. The WPDs have clear large south-north and small west-east patterns across the Amazon basin at the spatial and temporal scales. The degrees of *P*, *TWSA*, *DSR*, or *LAI* impact on *ET* are affected by drought events and the spatiotemporal scale. The northern and central of Amazon have fewer anthropic pressures and denser vegetation cover. Drought events enhance vegetation growth, which increases vegetation transpiration. In the southern water-limited area, drought events would intensify the impact of soil moisture/groundwater on *ET*. During the 2010 drought, *ET* was supported by both rainfall and deep soil moisture/groundwater to maintain the same yield compared to the wet years. After the drought, when the watershed was no longer water-limited, the deep soil moisture/groundwater had recovered and *ET* was not immediately supported by it. The WPD introduced in this study can well reflect this restoration process.

This study explored how rainfall, *TWSA*, radiation, and phenology drive *ET* in the Amazon basin. The results reflect the lag relationship between *ET* and these influencing factors, as well as the whole dynamic process of deep soil moisture/groundwater impact on *ET* in the drought. The vegetation phenology increases the complexity of the driving factor of *ET* in the Amazon. This study sheds light on the applicability of WPD in studying the driving factors of *ET* and expands its application prospect in the field of the hydrological cycle.

Acknowledgements

This research was partially supported by NSF project of China (41972244) and by the Director, Office Science, Office of Biological and Environmental Research of the U.S. Department of Energy under Contract DE-0010620 as part of their Earth System Modeling and NGEE-Tropics Program.

Open Research

[Data] *ET* data is derived from MODIS global terrestrial *ET* (MOD16A2) product, which is available from http://www.ntsg.umt.edu/project/mod16.

[Data] *TWSA* (RL05) is estimated by the most recent release of the spherical harmonics GRACE observations, which is available at http://grace.jpl.nasa.gov.

[Data] TRMM data is available from http://trmm.gsfc.nasa.gov/.

[Data] Radiation (Downward Shortwave Radiation, *DSR*) is provided by the MODIS Terra and Aqua combined Level 3 product (MCD18A1 Version 6.1). It is available at https://lpdaac.usgs.gov/products/mcd18a1v061/.

[Data] *LAI* (MCD15A2H, Collection 6) is available from https://lpdaac.usgs.gov/products/mcd15a2hv006/.

[Data] Land cover (MCD12Q2, Collection 6) information is available from https://lpdaac.usgs.gov/products/mcd12q2v006/.

[Software] Scripts used to process the dataset and calculate the results are available from the corresponding author upon reasonable request.

References:

Andreo, B., Jimenez, P., Duran, J. J., Carrasco, F., Vadillo, I., & Mangin, A. (2006). Climatic and hydrological variations during the last 117 – 166 years in the south of the Iberian Peninsula, from spectral and correlation analyses and continuous wavelet analyses. *Journal of Hydrology*, *324*, 24–39. https://doi.org/10.1016/j.jhydrol.2005.09.010

Aparecido, E., Matricardi, T., Skole, D. L., Olívia B. C., & Pereira, E. (2020). Long-term forest degradation surpasses deforestation in the Brazilian Amazon. *Science*, *369*(1378), 1382. https://doi.org/10.1126/science.abb3021

Audoin, B. & Roux, J. (1996). An innovative application of the Hilbert transform to time delay estimation of overlapped ultrasonic echoes. *Ultrasonics*, *34*(1), 8942-8949. https://doi.org/10.1016/0041-624X(95)00088-K

Baker, I. T., Prihodko, L., Denning, A. S., Goulden, M., Miller, S., & da Rocha, H. R. (2008). Seasonal drought stress in the Amazon: Reconciling models and observations. *Journal of Geophysical Research: Biogeoences*, *113*, 1–10. https://doi.org/10.1029/2007JG000644

Bjorklund, S. & Ljung, L. (2009). An improved phase method for time-delay estimation. *Automatica*, *45*(10), 2467-2470. https://doi.org/10.1016/j.automatica.2009.07.001

Bonan, G. B., Levis, S., Kergoat, L., & Oleson, K. W. (2002). Landscapes as patches of plant functional types: An integrating concept for climate and ecosystem models. *Global Biogeocheical Cycles*, *16*, 5-1-5-23. https://doi.org/10.1029/2000GB001360

Bonan, G. B., & Doney, S. C. (2018). Climate, ecosystems, and planetary futures: The challenge to predict life in Earth system models. *Science*, *359*, 6375

Brando, P. M., Goetz, S. J., Baccini, A., Nepstad, D. C., Beck, P. S. A., & Christman, M. C. (2010). Seasonal and interannual variability of climate and vegetation indices across the Amazon. *Proceedings of the National Academy of sciences of the United States of America*, *107*, 14685–14690. https://doi.org/10.1073/pnas.0908741107

Brando, P. M., Balch, J. K., Nepstad, D. C., Morton, D. C., Putz, F. E., Coe, M. T., Silvérioa, D., Macedo, M. N., Davidson, E. A., Nóbrega, C. C., Alencar, A., & Soares-Filho, B. S. (2014), Abrupt increases in Amazonian tree mortality due to drought-fire interactions, *Proceedings of the National Academy of Sciences of the United States of America*, *111*, 6347–6352. https://doi.org/ 10.1073/pnas.1305499111

Brown, D. S., Brown, J. C., & Brown, C. (2016). Land occupations and deforestation in the brazilian amazon. *Land Use Policy*, *54*, 331-338. https://doi.org/ 10.1016/j.landusepol.2016.02.003

Budyko, M. I. (1974). Climate and Life. Academic Press, New York.

Carter, G. C. (1993). Coherence and time delay estimation: an applied tutorial for research, development, test, and evaluation engineers. New York: IEEE Press, 1-27.

Carnicer, J., Barbeta, A., Seerlich, D., COll, M., & Penuelas, J. (2013). Contrasting trait syndromes in angiosperms on a large scale. *Front. Plant Science, 4*, 409. https://doi.org/10.3389/fpls.201.00409

Christoffersen, B. O., Restrepo-Coupe, N., Arain, M. A., Baker, I. T., Cestaro, B. P., Ciais, P., et al. (2014). Mechanisms of water supply and vegetation demand govern the seasonality and magnitude of evapotranspiration in Amazonia and Cerrado. *Agricultural and Forest Meteorology*, *191*, 33–50. https://doi.org/10.1016/j.agrformet.2014.02.008

Culf, A. D., Foken, T., & Gash, J. H. C. (2008). The energy balance closure problem: an overview. *Ecological Applications*, *18*, 1351-1367. https://doi.org/10.1890/06-0922.1

da Rocha, H. R., Manzi, A. O., Cabral, O. M., Miller, S. D., Goulden, M. L., & Saleska, S. R. (2009). Patterns of water and heat flux across a biome gradient from tropical forest to savanna in brazil. *Journal of Geophysical Research: Biogeoences*, *114*, 579-581. https://doi.org/10.1029/2007JG000640

Danko, D. M. (1992). The digital chart of the world. *Photogrammetric Engineering and Remote Sensing*, *58*. https://doi.org/10.1016/0924-2716(92)90041-7

De Oliveira, J. V., Ferreira, D. B. D. S., Sahoo, P. K., Sodré, G. R. C., De Souza, E. B., & Queiroz, J. C. B. (2018). Differences in precipitation and evapotranspiration between forested and deforested areas in the amazon rainforest using remote sensing data. *Environmental Earth Sciences*, *77*(6), 239. https://doi.org/ 10.1007/s12665-018-7411-9

Doughty, C. E., & Goulden, M. L. (2008). Seasonal patterns of tropical forest leaf area index and CO2 exchange. J*ournal of Geophysical Research: Biogeoscience*, *113*, n/a-n/a. https://doi/org/10.1029/2007JG000590

Doughty, C. E., Metcalfe, D. B., Girardin, C. A. J., Amézquita, F. F., Cabrera, D. G., Huasco, W. H., Silva-Espejo, J. E., Araujo-Murakami, A., da Costa, M. C., Rocha, W., Feldpausch, T.R., Mendoza, A. L. M., da Costa, A. C. L., Meir, P., Phillips, O. L., & Malhi, Y. (2015). Drought impact on forest carbon dynamics and fluxes in Amazonia. *Nature*, *519*, 78–82. https://doi.org/10.1038/nature14213

Doughty, R., Khler, P., Frankenberg, C., Magney, T. S., & Moore, B. (2019). Tropomi reveals dry-season increase of solar-induced chlorophyll fluorescence in the amazon forest. *Proceedings of the National Academy of Sciences*, *116*(44), 22393. https://doi.org/ 10.1073/pnas.1908157116

Doughty, R., Xiao, X., Qin, Y., Wu, X., & Moore, B. (2020). Small anomalies in dry-season greenness and chlorophyll fluorescence for amazon moist tropical forests during El Ni˜no and La Ni˜na. *Remote Sensing of Environment*, *253*. https://doi.org/10.1016/j.rse.2020.112196

Etter, D. M., & Stearns, S. D. (1981). Adaptive estimation of time delays in sampled data systems. *IEEE Transactions on Acoustics Speech and Signal Processing*, *29*(3), 582–587

Fang, K., Shen, C., Fisher, J. B., & Niu, J. (2016). Improving budyko curve-based estimates of long-term water partitioning using hydrologic signatures from grace. *Water Resources Research*, *52*(7), 5537–5554

Fassoni-Andrade, A. C., Fleischmann, A. S., Papa, F., Paiva, R. C. D. d., Wongchuig, S., Melack, J. M., Moreira, A. A., Paris, A., Ruhoff, A., Barbosa, C., Maciel, D. A., Novo, E., Durand, F., Frappart, F., Aires, F., Abrahão, G. M., Ferreira-Ferreira, J., Espinoza, J. C., Laipelt, L., Costa, M. H., Espinoza-Villar, R., & Calmant, S.. (2021). Amazon hydrology from space: Scientific advances and future challenges. *Reviews of Geophysics*, *59*, e2020RG000728. https://doi.org/10.1029/2020RG000728

Fisher, J. B., Malhi, Y., Bonal, D., da Rocha, H. R., & Randow, C. V. (2010). The land–atmosphere water flux in the tropics. Global C*hange Biology*, *15*(11), 2694-2714. https://doi.org/10.1111/j.1365-2486.2008.01813.x

Flantua, S. G. A., Hooghiemstra, H., Vuille, M., Behling, H., Carson, J. F., Gosling,W. D., Hoyos, I., Ledru, M. P., Montoya, E., Mayle, F., Maldonado, A., Rull, V., Tonello, M. S., Whitney, B. S., & González-Arango, C. (2015). Climate variability and human impact on the environment in South America during the last 2000 years: synthesis and perspectives. *Climate of the Past Discussions*, *11*, 3475–3565. https://doi.org/10.5194/cpd-11-3475-2015.

Friedl, M., Gray, J., & Sulla-Menashe, D. (2019). [Dataset] MCD12Q2 MODIS/Terra+Aqua Land Cover Dynamics Yearly L3 Global 500m SIN Grid V006. NASA EOSDIS Land Processes DAAC. Accessed 2021-09-15 from https://doi.org/10.5067/MODIS/MCD12Q2.006

Fu, R., & Li, W. (2004). The influence of the land surface on the transition from dry to wet season in Amazonia. *Theoretical and Applied Climatology*, *78*, 97–110. https://doi.org/10.1007/s00704-004-0046-7

Gentine, P. P., D'Odorico, B. R., Lintner, G. S., & Salvucci, G. (2012). Interdependence of climate, soil, and vegetation as constrained by the Budyko curve. *Geophysical Research Letters, 39*, L19404. https://doi.org/10.1029/2012GL053492

Gonçalves, N. B., Lopes, A. P., Dalagnol, R., Wu, J., Pinho, D. M., & Nelson, B. W. (2020). Both. near-surface and satellite remote sensing confirm drought legacy effect on tropical forest leaf phenology after 2015/2016 ENSO drought. *Remote Sensing of Environment*, *237*. https://doi.org/10.1016/j.rse.2019.111489

Hasler, N., & Avissar, R. (2006). What controls evapotranspiration in the amazon basin? *Journal of Hydrometeorology*, *8*, 380–395. https://doi.org/10.1175/JHM587.1

Hilker, T., Lyapustin, A. I., Tucker, C. J., Hall, F. G., Myneni, R. B., Wang, Y., Bi, J., de Moura, Y. M., & Sellers, P. J. (2014). Vegetation dynamics and rainfall sensitivity of the Amazon. *Proceedings of the National Academy of sciences of the United States of America*, *111*, 16041–16046. https://doi.org/10.1073/pnas.1404870111

Huffman, G. J., Bolvin, D. T., Nelkin, E. J., Wolff, D. B., Adler, R. F., Gu, G., Hong, Y., Bowman, K. P., & Stocker, E. F. (2007). [Dataset] The TRMM multi-satellite precipitation analysis: Quasi-global, multi-Year, combined-Sensor precipitation estimates at fine scale. *Journal of Hydrometeorology, 8*(1), 38-55. https://doi.org/10.1175/jhm560.1

Humphrey, V., Zscheischler, J., Ciais, P., Cudmundsson, L., Sitch, S., & Seneviratne, S. I. (2018). Sensitivity of atmospheric CO2 growth rate to observed changes in terrestrial water storage. *Nature*, *560*, 628–631. https://doi.org/10.1038/s41586-018-0424-4

Juárez, R. I.N., Hodnett, M. G., Fu, R., Goulden, M. L., & von Randow, C. (2007). Control of dry season evapotranspiration over the Amazonian forest as inferred from observations at a southern Amazon forest site. J*ournal of Climate*, *20*, 2827–2839. https://doi.org/10.1175/JCLI4184.1.

Labat, D. (2005). Recent advances in wavelet analyses: Part 1. A review of concepts. *Journal of Hydrology*, *314*, 275–288. https://doi.org/10.1016/j.jhydrol.2005.04.003

Labat, D., Ronchail, J., & Guyot, J. L. (2005). Recent advances in wavelet analyses: Part 2—Amazon, Parana, Orinoco and Congo discharges time scale variability. *Journal of Hydrology*, *314*, 289–311. https://doi.org/10.1016/j.jhydrol.2005.04.004

Landerer, F. W., & Swenson, S. C. (2012). Accuracy of scaled GRACE terrestrial water storage estimates. *Water Resources Research*, *48*, W04531. https://doi.org/10.1029/2011WR011453

Landerer, F. (2021). [Dataset] TELLUS_GRAC_L3_CSR_RL06_LND_v04. Ver. RL06 v04. PO. DAAC, CA, USA. Accessed 2016-09-13 at https://doi.org/10.5067/TELND-3AC64

Lin, Y. H., Lo, M. H., & Chou, C. (2016). Potential negative effects of groundwater dynamics on dry season convection in the amazon river basin. *Climate Dynamics*, *46*(3), 1001–1013. https://doi.org/10.1007/s00382-015-2628-8

Liu, D., Wang, G., Mei, R., Yu, Z., & Yu, M. (2014). Impact of initial soil moisture anomalies on. climate mean and extremes over Asia. *Journal of Geophysical Research-Atmospheres*, *119*(2), 529–545. https://doi.org/10.1002/2013JD020890

Liu, Y. Y., Dijk, A. I. J. M. V., Miralles, D. G., Mccabe, M. F., & Restrepo-Coupe, N. (2018). Enhanced canopy growth precedes senescence in 2005 and 2010 Amazonian droughts. *Remote Sensing of Environment*, *211*, 26–37. https://doi.org/10.1016/j.rse.2018.03.035

Maeda, E. E., Ma, X., Wagner, F. H., Kim, H., Oki, T., Eamus, D., & Huete, A. (2017). Evapotranspiration seasonality across the Amazon Basin. *Earth System Dynamics Discussions*, *8*, 439–454. https://doi.org/ 10.5194/esd-2016-75

Malhi, Y., Pegoraro, E., Nobre, A. D., Pereira, M. G. P., Grace, J., Culf, A. D., & Clement, R. (2002). Energy and water dynamics of a central Amazonian rain forest. *Journal of Geophysical Research: Atmospheres*, *107*, 8061. https://doi.org/10.1029/2001JD000623

Maskell, D. L., & Woods, G. S. (2002). The discrete-time quadrature subsample estimation of delay. *Instrumentation & Measurement IEEE Transactions on*, *51*(1), 133–137. https://doi.org/10.1109/19.989916

Mayorga, E., Logsdon, M. G., Ballester, M. V. R., & Richey, J. E. (2005). Estimating cell-to-cell land surface drainage paths from digital channel networks, with an application to the Amazon basin. *Journal of Hydrology*, *315*, 167–182. https://doi.org/10.1016/j.jhydrol.2005.03.023

Medvigy, D., Walko, R. L., & Avissar, R. (2011). Effects of deforestation on spatiotemporal distributions of precipitation in South America, *Journal of Climate*, *24*(8), 2147–2163. https://doi.org/10.1175/2010JCLI3882.1

Micheletti, R. (1991). Phase angle measurement between two sinusoidal signals. *Instrumentation & Measurement IEEE Transactions on*, *40*(1), 40–42. https://doi.org/10.1109/19.69948

Miguez-Macho, G., & Fan, Y. (2012a). The role of groundwater in the Amazon water cycle: 1. Influence on seasonal streamflow, flooding and wetlands. *Journal of Geophysical Research: Atmospheres*, *117*, 1–30. https://doi.org/10.1029/2012JD017539

Miguez-Macho, G., & Fan, Y. (2012b). The role of groundwater in the Amazon water cycle: 2. Influence on seasonal soil moisture and evapotranspiration. *Journal of Geophysical Research: Atmospheres*, *117*, D15114. https://doi.org/10.1029/2012JD017540

Miguez-Macho, G., & Fan, Y. (2021). Spatiotemporal origin of soil water taken up by vegetation. *Nature*, *598*, 624-628. https://doi.org/10.1038/s41586-021-03958-6

Moura, M. M., dos Santos, A. R., Pezzopane, J. E. M., Alexandre, R. S., da Silva, S. F., Pimentel, S. M., de Andrade, M. S. S., Silva, F. G. R., Branco, E. R. F., Moreira, T. R., da Silva, R. G., & de Carvalho, J. R. (2019). Relation of El Niño and La Niña phenomena to precipitation, evapotranspiration and temperature in the Amazon basin, *Science of The Total Environment*, *651*, 1639–1651. https://doi.org/10.1016/j.scitotenv.2018.09.242

Mu, Q., Zhao, M., & Running, S.W. (2011). [Dataset] Improvements to a MODIS global terrestrial evapotranspiration algorithm. *Remote Sensing of Environment*, *115*, 1781–1800. https://doi.org/10.1016/j.rse.2011.02.019

Myneni, R., Knyazikhin, Y., Park, T. (2015). [Dataset] MCD15A2H MODIS/Terra+Aqua Leaf Area Index/FPAR 8-day L4 Global 500m SIN Grid V006. NASA EOSDIS Land Processes DAAC. Accessed 2021-09-15 from https://doi.org/10.5067/MODIS/MCD15A2H.006

Niu, J., Shen, C., Chambers, J Q., Melack, J. M., & Riley, W. J. (2017). Interannual variation in hydrologic budgets in an Amazonian watershed with a coupled subsurface - land surface process model. *Journal of Hydrometeorology*, *18*, 2597–2617. https://doi.org/10.1175/JHM-D-17-0108.1

Qin, Y., Xiao, X., Dong, J., Zhou, Y., & Moore, B. (2017). Annual dynamics of forest areas in south America during 2007–2010 at 50-m spatial resolution. *Remote Sensing of Environment*, *201*, 73–87. https://doi.org/10.1016/j.rse.2017.09.005

Restrepo-Coupe, N., Levine, N. M., Christoffersen, B. O., Albert, L. P., Wu, J., Costa, M. H., Galbraith, D., Imbuzeiro, H., Martins, G., da Araujo, A C., Malhi, Y. S., Zeng, X., Moorcroft, P., & Saleska, S. R. (2016). Do dynamic global vegetation models capture the seasonality of carbon fluxes in the Amazon basin? A data-model intercomparison. *Global Change Biology*, *23*, 191–208. https://doi.org/10.1111/gcb.13442

Saleska, S. R., Miller, S. D., Matross, D. M., Goulden, M. L., Wofsy, S. C., da Rocha, H. R., de Camargo, P. B., Crill, P., Daube, B. C., de Freitas, H. C., Hutyra, L., Keller, M., Kirchhoff, V., Menton, M., Munger, J. W., Pyle, E. H., Rice, A. H., & Silva, H. (2003). Carbon in Amazon forests: unexpected seasonal fluxes and disturbance-induced losses. *Science*, *302*, 1554–1557. https://doi.org/10.1126/science.1091165

Saleska, S. R., Didan, K., Huete, A. R., & da Rocha, H. R. (2007). Amazon forests green-up during 2005 drought. *Science*, *318*, 612. https://doi.org/ 10.1126/science.1146663

Samanta, A., Knyazikhin, Y., Xu, L., Dickinson, R. E., Fu, R., Costa, M. H., Saatchi, S. S., Nemani, R. R., & Myneni, R. B. (2012). Seasonal changes in leaf area of Amazon forests from leaf flushing and abscission. *Journal of Geophysical Research: Biogeoences*, *117*, 75–81. https://doi.org/10.1029/2011JG001818

Schaefli, B., Maraun, D., & Holschneider, M. (2007). What drives high flow events in the Swiss Alps? Recent developments in wavelet spectral analysis and their application to hydrology. *Advances in Water Resources*, *30*, 2511–2525. https://doi.org/10.1016/j.advwatres.2007.06.004

So, H. C. (2006). A comparative study of two discrete-time phase delay estimators. *IEEE Transactions on Instrumentation & Measurement*, *54*(6), 2501–2504. https://doi.org/10.1109/TIM.2005.859143

Spracklen, D. V., Arnold, S. R., & Taylor, C. M. (2012). Observations of increased tropical rainfall preceded. by air passage over forests. *Nature*, *489*, 282–285. https://doi.org/10.1038/nature11390

Staal, A., Flores, B. M., Aguiar, A. P., Bosmans, J., & Tuinenburg, O. A. (2020). Feedback between drought and deforestation in the Amazon. *Environmental Research Letter*s, *15*, 044024. https://doi.org/10.31223/osf.io/8rq4n

Swann, A. L. S., & Koven, C. D. (2017). A direct estimate of the seasonal cycle of evapotranspiration over the amazon. basin. *Journal of Hydrometeorology*, *18*(8), 2173–2185. https://doi.org/10.1175/JHM-D-17-0004.1

Swenson, S. C., & Wahr, J. (2006). Post-processing removal of correlated errors in GRACE data. *Geophysical Research Letters*, *33*, L08402. https://doi.org/10.1029/2005GL025285

Tang, J., Riley, W. J., & Niu, J. (2015). Incorporating root hydraulic redistribution in CLM4.5: Effects on predicted site and global evapotranspiration, soil moisture, and water storage. *Journal of Advances in Modeling Earth Systems*, *7*, 1828–1848. https://doi.org/10.1002/2015MS000484

Torrence, C., & Compo, G. P. (1998). A Practical Guide to Wavelet Analysis. *Bulletin of the American Meteorological Society*, *79*, 61–78. https://doi.org/10.1175/1520-0477(1998)079<0061:APGTWA>2.0. CO;2

Verbeeck H, Peylin P, Bacour C, Bonal, D., Steppe, K., & Ciais, P. (2011). Fluxes in Amazon forests: Fusion of eddy covariance data and the ORCHIDEE model. *Journal of Geophysical Research*, *116*(G2), G02018. https//doi.org/10.1029/2010jg001544

Wang, D. (2012). Evaluating interannual water storage changes at watersheds in Illinois based on long-term soil moisture and groundwater level data. *Water Resources Research*, *48*(3), 31–40. https://doi.org/10.1029/ 2011wr010759

Wang, D. (2021). [Dataset] MODIS/Terra+Aqua Surface Radiation Daily/3-Hour L3 Global 1km SIN Grid V061. NASA EOSDIS Land Processes DAAC. Accessed 2021-09-15 from https://doi.org/10.5067/MODIS/MCD18A1.061

Wagner, F. H., Hérault, B., Bonal, D., Stahl, C., Anderson, L. O., Baker, T. R., et al. (2016). Climate seasonality limits leaf carbon assimilation and wood productivity in tropical forests. *Biogeoence*, *13*, 2537–2562. https://doi.org/10.5194/bg-13-2537-2016

Werth, D., & Avissar, R. (2004). The regional evapotranspiration of the Amazon. *Journal of Hydrometeorology*, *5*(1), 100–109. https://doi.org/10.1175/1525-7541(2004)005<0100:treota>2.0.co;2

Wongchuig, S., Espinoza, J. C., Condom, T., Segura, H., Ronchail, J., Arias, P. A., Junquas, C., Rabatel, A., & Lebel, T. (2021) A regional view of the linkages between hyddro-climatic changes and deforestation in the Southern Amazon. *International Journal of Climatology*. https://doi.org/ 10.1002/joc.7443

Yan, K., Park, T., Yan, G., Chen, C., Yang, B., Liu, Z., anemani, R. R., Knyazikhin, Y., & Myneni, R. B. (2016). Evaluation of MODIS LAI/FPAR product collection 6. Part 1: consistency and improvements. Remote Sensing, *8*(5), 359. https://doi.org/10.3390/rs8050359

Yang, D., Sun, F., Liu, Z., Cong, Z., Ni, G., & Lei, Z. (2007). Analyzing spatial and temporal variability of annual water-energy balance in nonhumid regions of China using the Budyko hypothesis. *Water Resources Research*, *43*, 436–451. https://doi.org/10.1029/2006WR005224

Yuan, W., Zheng, Y., Piao, S., Ciais, P., & Yang, S. (2019). Increased atmospheric vapor pressure deficit reduces global vegetation growth. *Science Advances*, *5*(8*)*, eaas1396. https://doi.org/10.1126/sciadv.aax1396

Zemp, D. C., Schleussner, C. F., Barbosa, H. M. J., & Rammig, A. (2017). Deforestation effects on Amazon. forest resilience. *Geophysical Research Letters*, *44*, 6182–6190. https://doi.org/10.1002/2017GL072955

Zhang, J., Hao, Y., Hu, X., Huo, X., & Hao, P. (2017). The effects of monsoons and climate teleconnections on the Niangziguan Karst Spring discharge in North China. *Climate Dynamics*, *48*(1-2), 53–70. https://doi.org/10.1007/ s00382-016-3062-2

Zhang, L., Dawes, W. R., & Walker, G. R. (2001). Response of mean annual evapotranspiration to vegetation. changes at catchment scale. *Water Resources Research*, *37*, 701–708. https://doi.org/10.1029/2000WR 900325

Figures

Figure 1. Contour plots of wavelet power spectra of precipitation (a), *ET* (b), *TWSA* (c), *DSR* (d), and *LAI* (e), and global wavelet spectra of precipitation (f), *ET* (g), *TWSA* (h), *DSR* (i), and *LAI* (j). The x-axes of subplots (a), (b), (c), (d), and (e) represent the time, the y-axis represents the periodicity scale, and the color represents the magnitude of the wavelet coefficient. The contour lines enclose regions of greater than 95% confidence (Torrence & Compo, 1998). The x-axes of subplots (f), (g), (h), (i), and (j) represent the power of global wavelet spectrum.

Figure 2. Cross wavelet power spectra of *ET* and *P* (a), *ET* and *TWSA* (b), *ET* and *DSR* (c), and *ET* and *LAI* (d). The contour plots represent the power of cross spectra and are shown as blank when the values are smaller than 2^{-8}. The arrows represent the phase relationship between these time series and are only presented when the wavelet power is greater than 2^{-2}.

Figure 3. Plots of phase differences (a) ϕ_{ET-P}^{Amazon}, $\phi_{ET-TWSA}^{Amazon}$, ϕ_{ET-DSR}^{Amazon}, and ϕ_{ET-LAI}^{Amazon}; (b) monthly time series data and (c) annual averaged data of *P* on the left y-axis, as well as *ET* on the right y-axis. All-time series data and phase differences are spatially-averaged across the Amazon basin.

Figure 4. Map of the pixel-by-pixel phase difference between *ET* and *P* ($\phi_{ET-P}^{1-degree}$) for each year from 2002 to 2013. Different colors represent different phase differences in time (month) as shown in the legend. Missing data from either *ET* or *P* are shown as blank.

Figure 5. Map of the pixel-by-pixel phase difference between *ET* and *TWSA* ($\phi_{ET-TWSA}^{1-degree}$) for each year from 2002 to 2013.

Figure 6. Map of the pixel-by-pixel phase difference between *ET* and *DSR* ($\phi_{ET-DSR}^{1-degree}$) for each year from 2002 to 2013.

Figure 7. Map of the pixel-by-pixel phase difference between *ET* and *LAI* ($\phi_{ET-LAI}^{1-degree}$) for each year from 2002 to 2013.

Figure 8. The Budyko framework applied to 33 sub-basins of Amazon. In each subplot, the x-axes are the ratio between potential evapotranspiration and precipitation (*PET / P*); the y-axes are the ratio between actual ET and precipitation (*ET / P*); the solid horizontal line indicates water limitation (i.e., annual *ET* = annual *P*); the 1:1 line indicates energy limitation (annual *ET* = annual *PET*); the dashed vertical line indicates the boundary between these limitations; and the dots are the annual averaged data for each sub-basin. The label of each subplot corresponds to the index of each sub-basin (see Figure S1) and the positions of them are generally corresponding to the geographical location of each sub-basin.

Figure 9. Plots of (a) phases between *ET* and *P* ($\phi_{ET-P}^{Zone\,1}$), between *ET* and *TWSA* ($\phi_{ET-TWSA}^{Zone\,1}$), between *ET* and *DSR* ($\phi_{ET-DSR}^{Zone\,1}$), and between *ET* and *LAI* ($\phi_{ET-LAI}^{Zone\,1}$); (b) monthly time series of *P*, *DSR*, and *ET*; and (c) annual averages of *P* and *ET*. All-time series data are spatially averaged over Zone 1, and the phases are calculated based on the spatially averaged monthly variables of Zone 1.

Figure 10. Plots of (a) phases between *ET* and *P* ($\phi_{ET-P}^{Zone\ 2}$), and between *ET* and *TWSA* ($\phi_{ET-TWSA}^{Zone\ 2}$), between *ET* and *DSR* ($\phi_{ET-DSR}^{Zone\ 2}$), and between *ET* and *LAI* ($\phi_{ET-LAI}^{Zone\ 2}$); (b) monthly time series of *P*, *DSR*, and *ET*; and (c) annual averages of *P* and *ET*. All-time series data are spatially averaged over Zone 2, and the phases are calculated based on the spatially averaged monthly variables of Zone 2.

Figure 11. Plots of (a) phases between *ET* and *P* ($\phi_{ET-P}^{Zone\ 3}$), and between *ET* and *TWSA* ($\phi_{ET-TWSA}^{Zone\ 3}$), between *ET* and *DSR* ($\phi_{ET-DSR}^{Zone\ 3}$), and between *ET* and *LAI* ($\phi_{ET-LAI}^{Zone\ 3}$); (b) monthly time series of *P*, *DSR*, and *ET*; and (c) annual averages of *P* and *ET*. All-time series data are spatially averaged over Zone 3, and the phases are calculated based on the spatially averaged monthly variables of Zone 3.

Figure 12. Plots of (a) phases between *ET* and *P* ($\phi_{ET-P}^{Zone\ 4}$), and between *ET* and *TWSA* ($\phi_{ET-TWSA}^{Zone\ 4}$), between *ET* and *DSR* ($\phi_{ET-DSR}^{Zone\ 4}$), and between *ET* and *LAI* ($\phi_{ET-LAI}^{Zone\ 4}$); (b) monthly time series of *P*, *DSR*, and *ET*; and (c) annual averages of *P* and *ET*. All-time series data are spatially averaged over Zone 4, and the phases are calculated based on the spatially averaged monthly variables of Zone 4.

Figure 1.

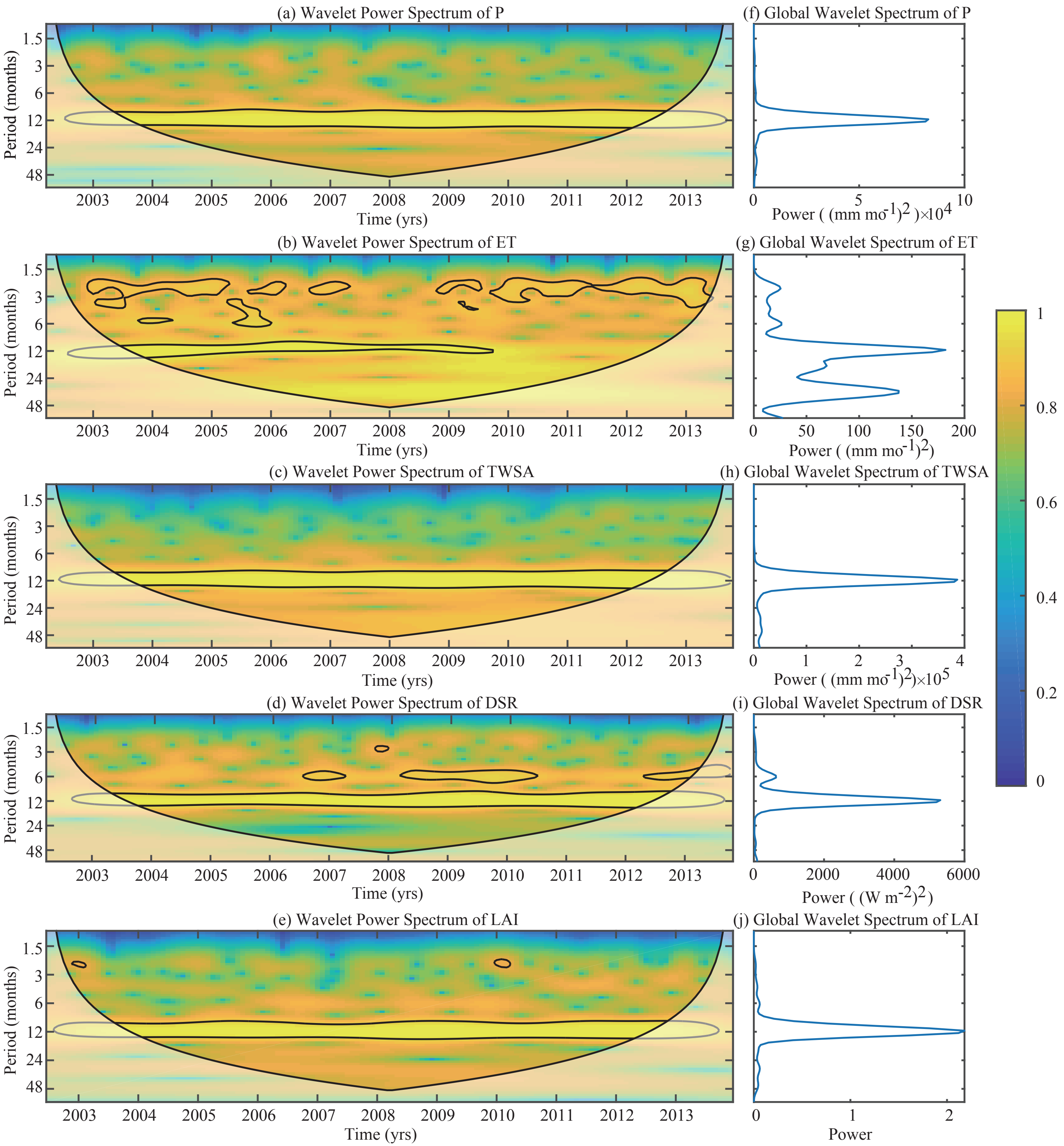

(a) Wavelet Power Spectrum of P
(b) Wavelet Power Spectrum of ET
(c) Wavelet Power Spectrum of TWSA
(d) Wavelet Power Spectrum of DSR
(e) Wavelet Power Spectrum of LAI
(f) Global Wavelet Spectrum of P
(g) Global Wavelet Spectrum of ET
(h) Global Wavelet Spectrum of TWSA
(i) Global Wavelet Spectrum of DSR
(j) Global Wavelet Spectrum of LAI
Period (months)
Time (yrs)
Power ((mm mo-1)2)×104
Power ((mm mo-1)2)
Power ((mm mo-1)2)×105
Power ((W m-2)2)
Power

Figure 2.

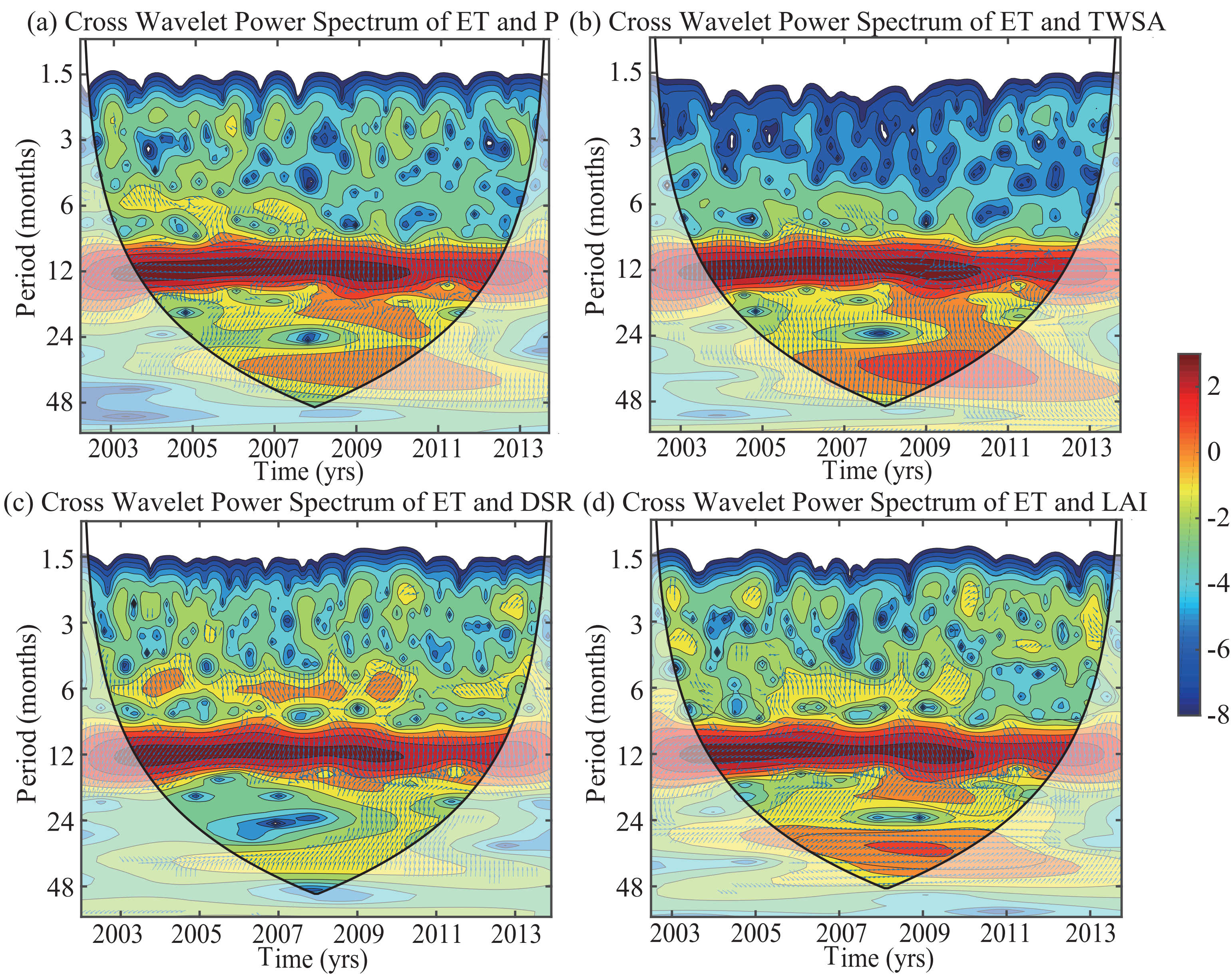

(a) Cross Wavelet Power Spectrum of ET and P
(b) Cross Wavelet Power Spectrum of ET and TWSA
(c) Cross Wavelet Power Spectrum of ET and DSR
(d) Cross Wavelet Power Spectrum of ET and LAI
Period (months)
1.5
3
6
12
24
48
Time (yrs)
2003
2005
2007
2009
2011
2013
2
0
-2
-4
-6
-8

Figure 3.

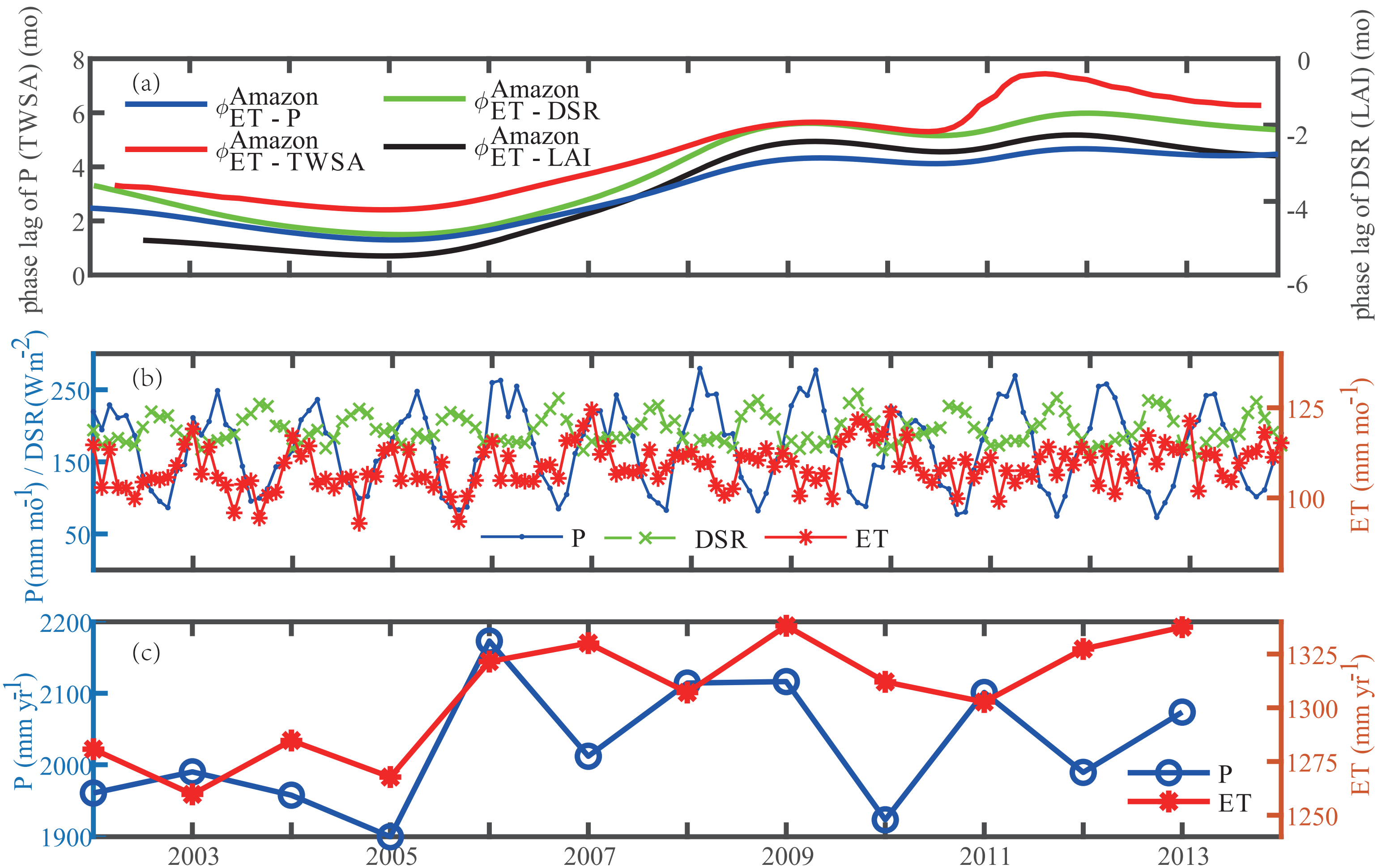

(a)
ϕ_{ET-P}^{Amazon}
$\phi_{ET-TWSA}^{Amazon}$
ϕ_{ET-DSR}^{Amazon}
ϕ_{ET-LAI}^{Amazon}
phase lag of P (TWSA) (mo)
phase lag of DSR (LAI) (mo)
(b)
P
DSR
ET
P (mm mo^{-1}) / DSR (W m^{-2})
ET (mm mo^{-1})
(c)
P
ET
P (mm yr^{-1})
ET (mm yr^{-1})
2003
2005
2007
2009
2011
2013

Figure 4.

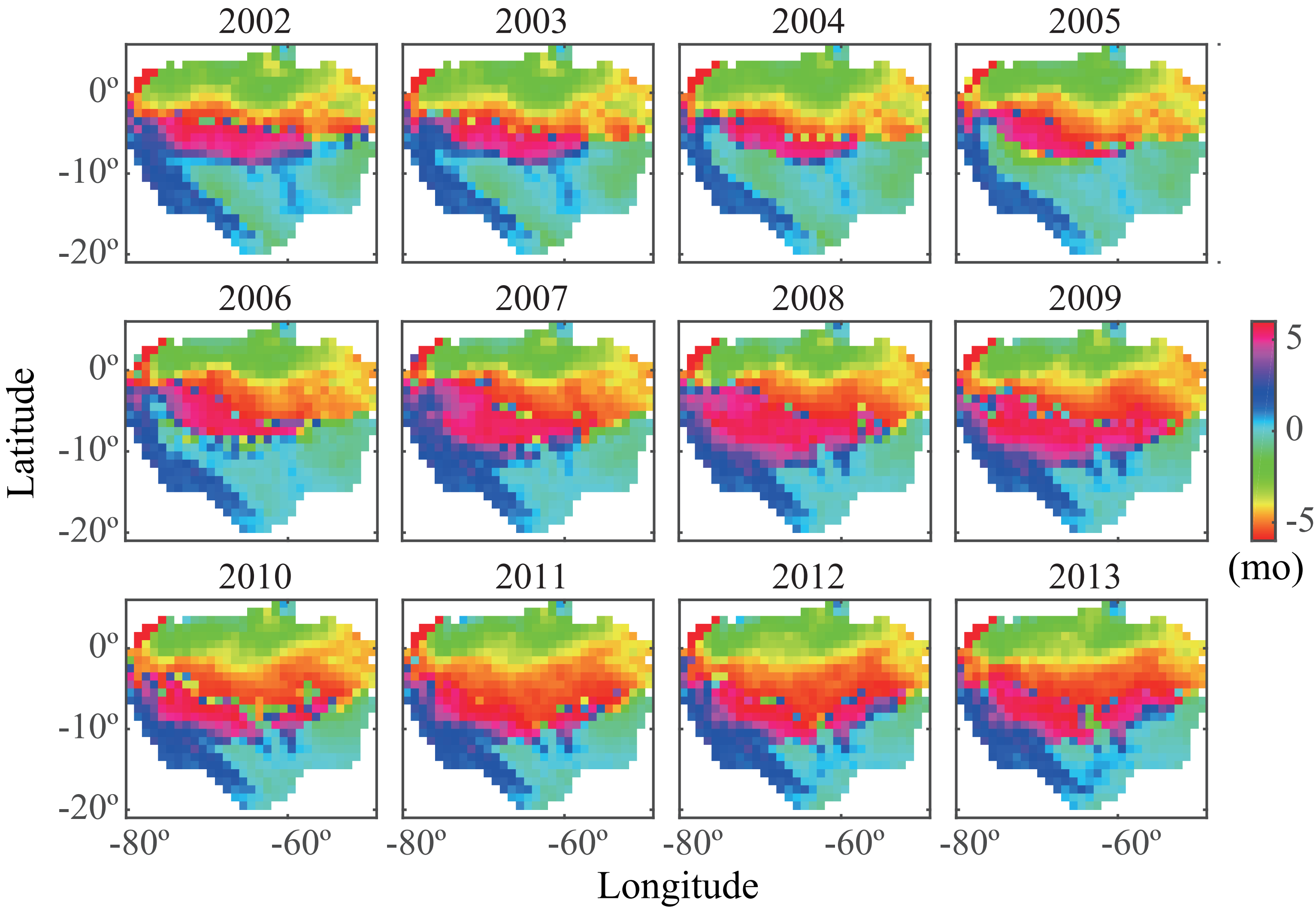

2002
2003
2004
2005
2006
2007
2008
2009
2010
2011
2012
2013
0º
-10º
-20º
-80º
-60º
Latitude
Longitude
5
0
-5
(mo)

Figure 5.

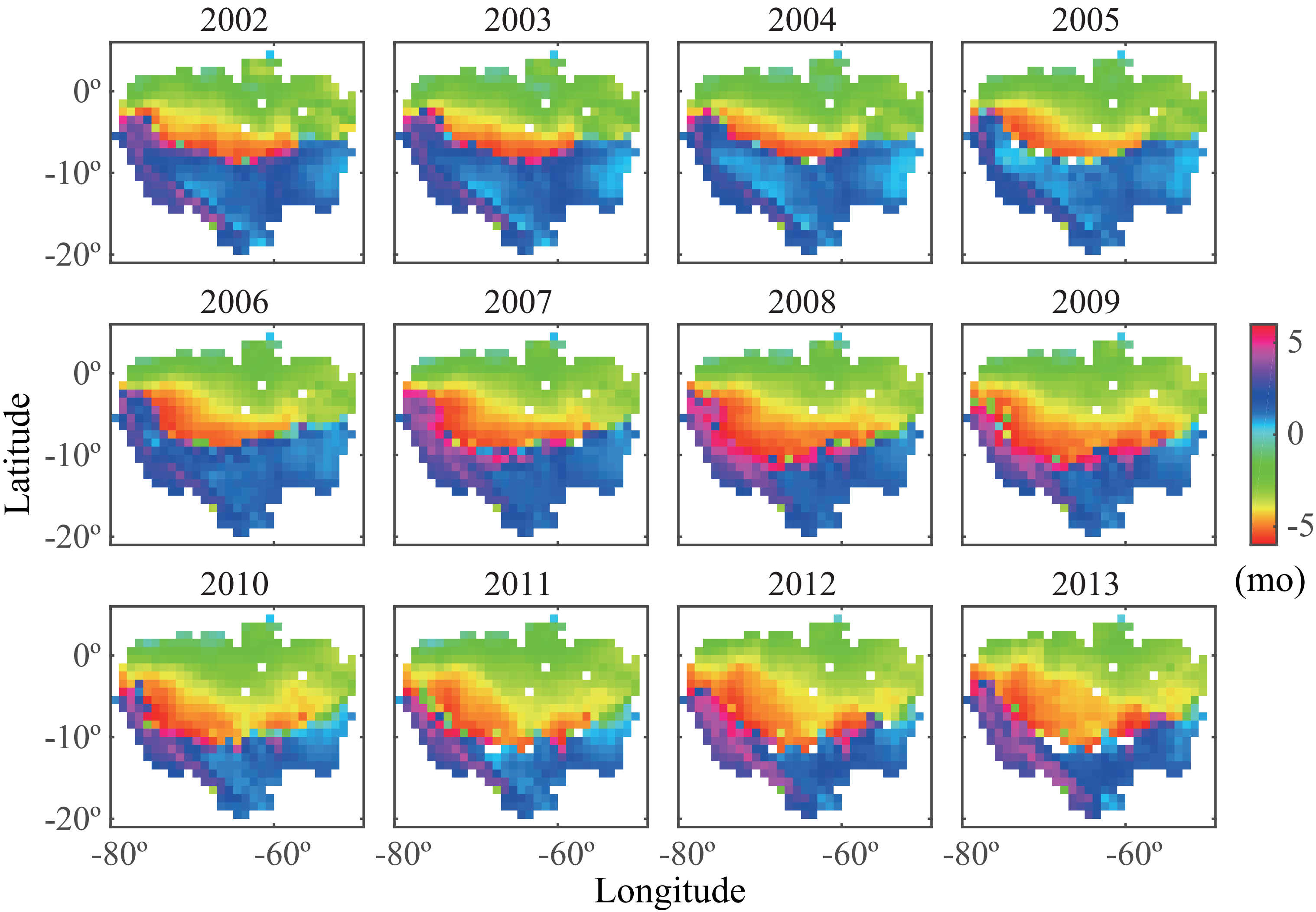
2002
2003
2004
2005
2006
2007
2008
2009
2010
2011
2012
2013
0º
-10º
-20º
-80º
-60º
Latitude
Longitude
5
0
-5
(mo)

Figure 6.

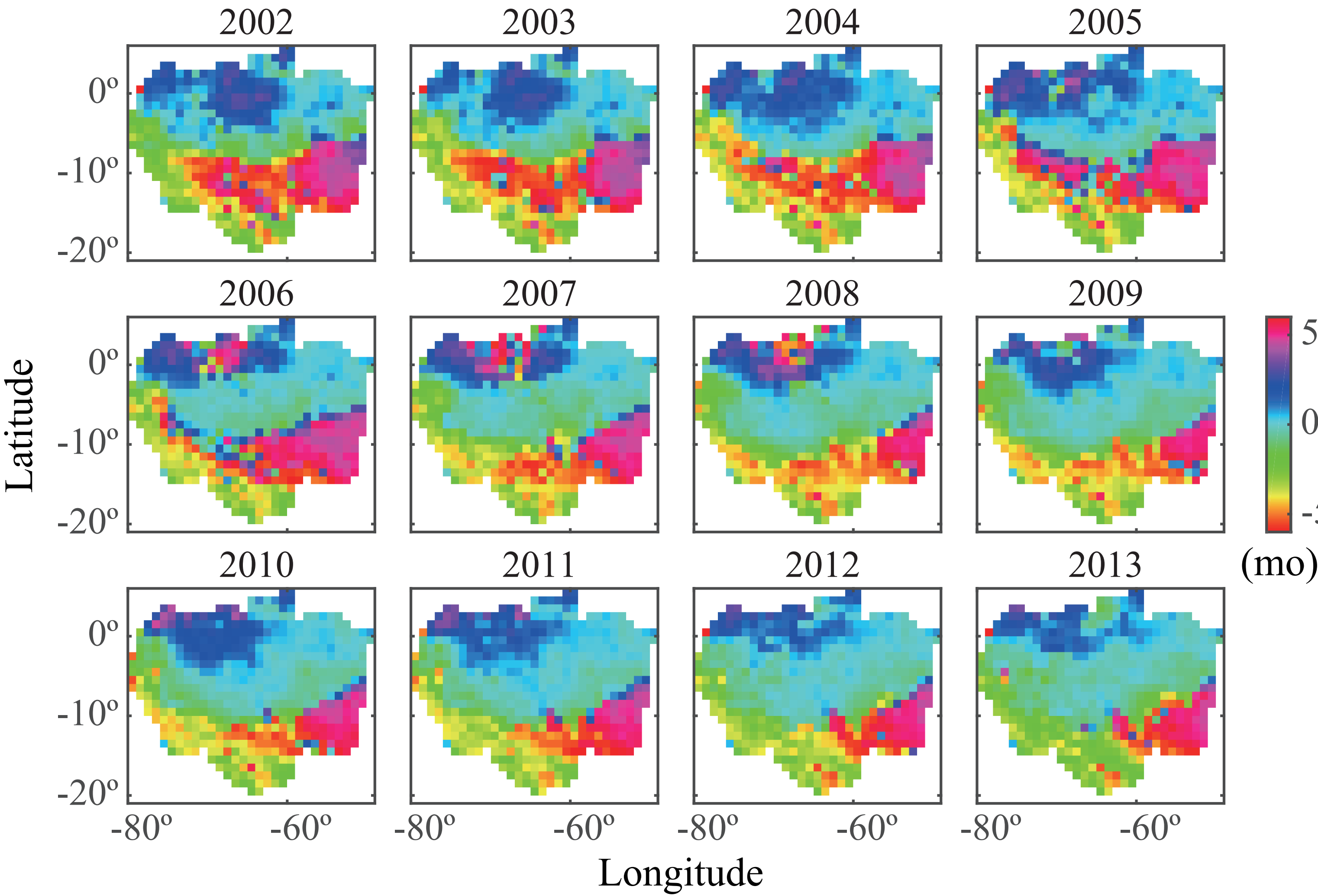

2002
2003
2004
2005
2006
2007
2008
2009
2010
2011
2012
2013
0º
-10º
-20º
-80º
-60º
Latitude
Longitude
5
0
-5
(mo)

Figure 7.

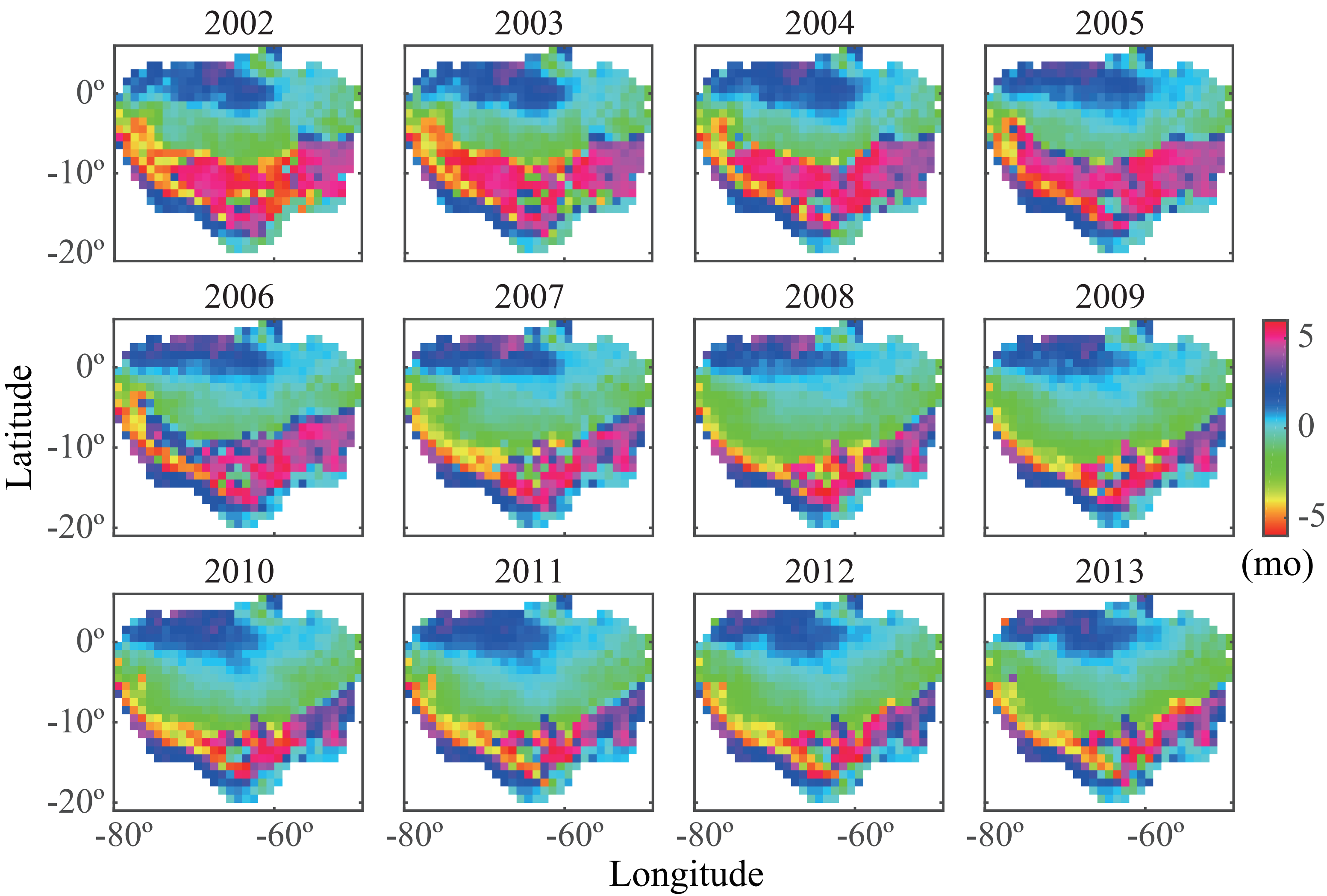
2002
2003
2004
2005
2006
2007
2008
2009
2010
2011
2012
2013
0º
-10º
-20º
-80º
-60º
Latitude
Longitude
5
0
-5
(mo)

Figure 8.

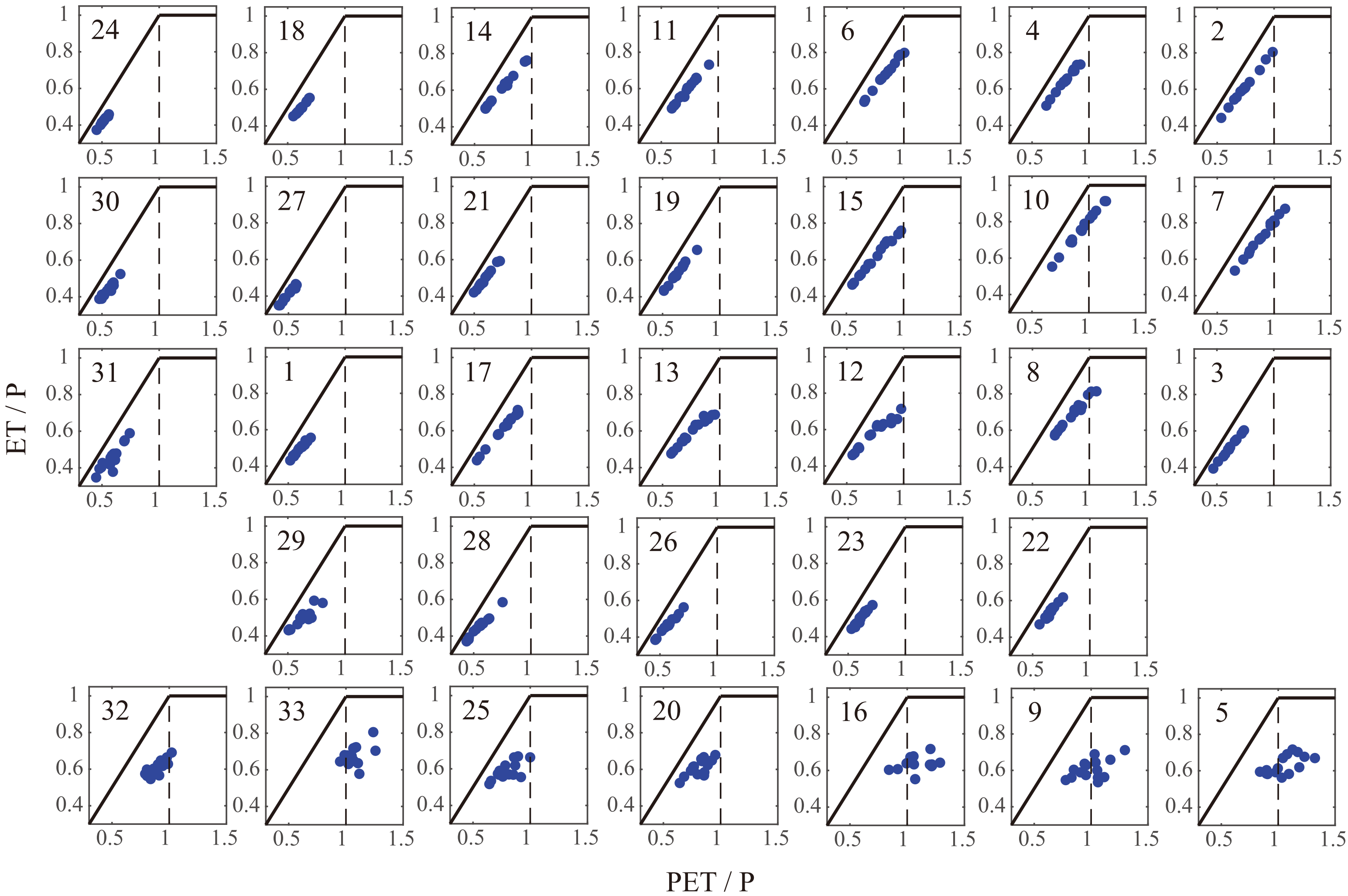
24
18
14
11
6
4
2
30
27
21
19
15
10
7
31
1
17
13
12
8
3
29
28
26
23
22
32
33
25
20
16
9
5
ET / P
PET / P

Figure 9.

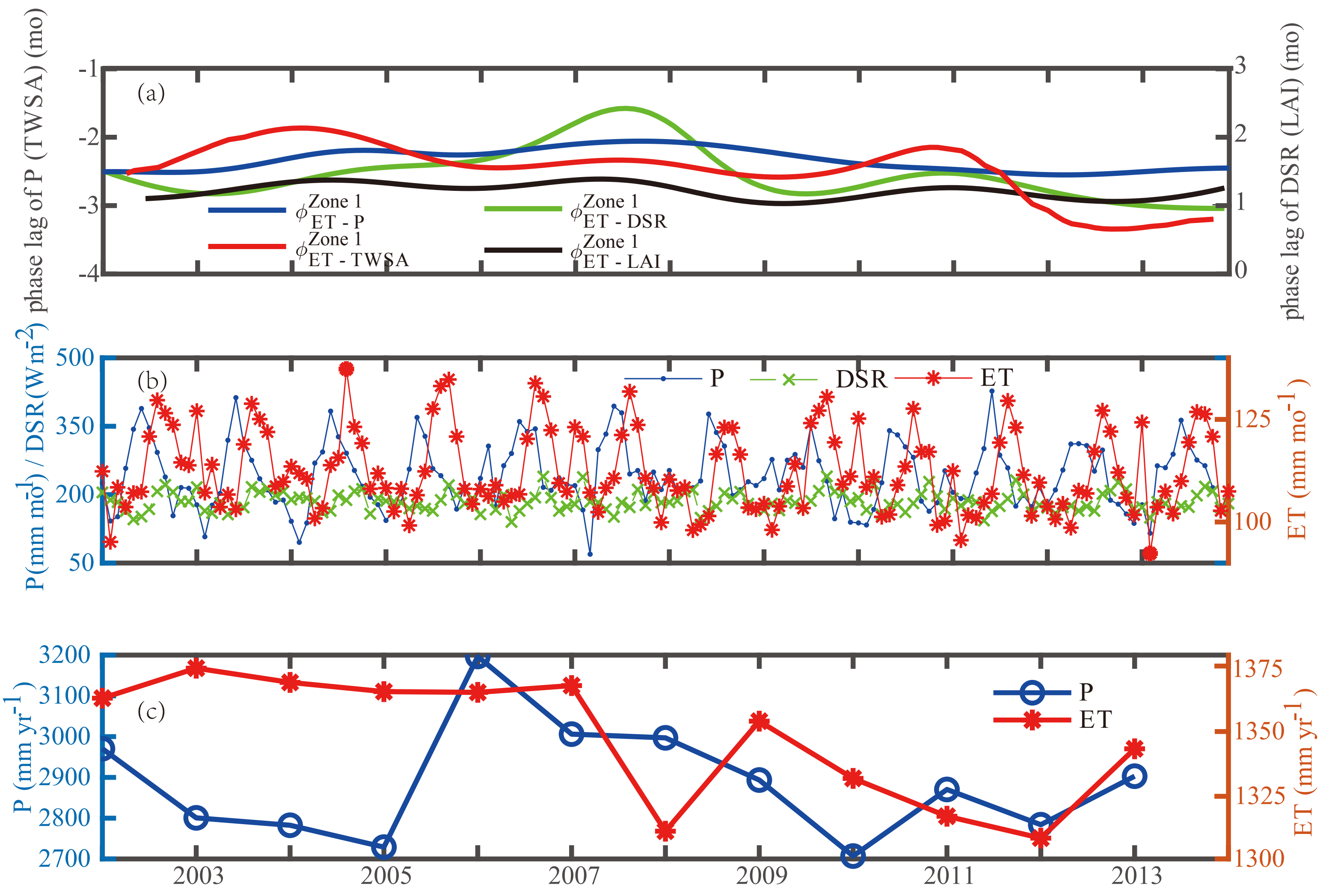

(a)
(b)
(c)
phase lag of P (TWSA) (mo)
phase lag of DSR (LAI) (mo)
$\phi^{Zone\ 1}_{ET - P}$
$\phi^{Zone\ 1}_{ET - DSR}$
$\phi^{Zone\ 1}_{ET - TWSA}$
$\phi^{Zone\ 1}_{ET - LAI}$
P
DSR
ET
P(mm mo^{-1}) / DSR(W m^{-2})
ET (mm mo^{-1})
P (mm yr^{-1})
ET (mm yr^{-1})
2003
2005
2007
2009
2011
2013

Figure 10.

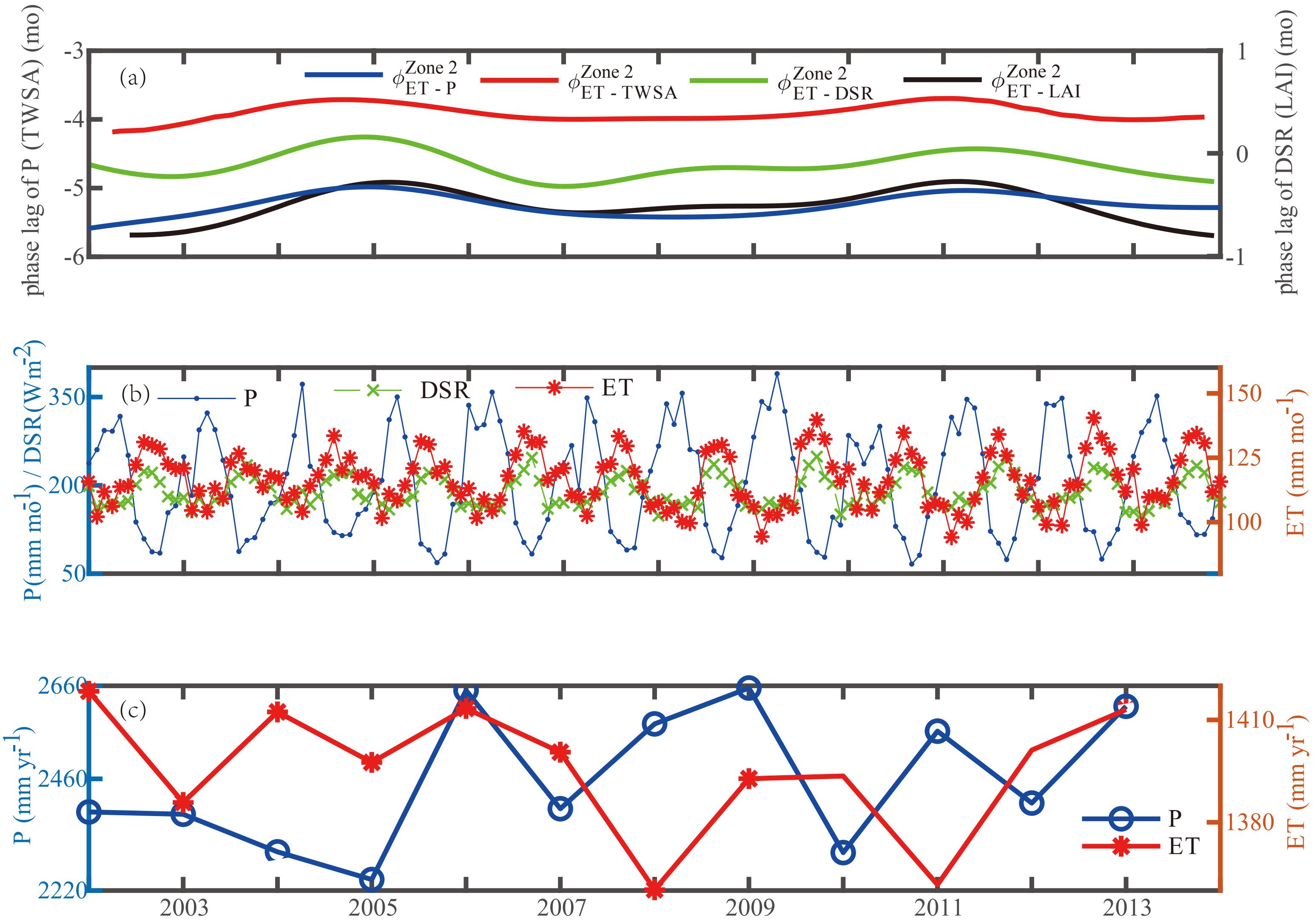

(a)
$\phi^{Zone\ 2}_{ET\ -\ P}$
$\phi^{Zone\ 2}_{ET\ -\ TWSA}$
$\phi^{Zone\ 2}_{ET\ -\ DSR}$
$\phi^{Zone\ 2}_{ET\ -\ LAI}$
phase lag of P (TWSA) (mo)
phase lag of DSR (LAI) (mo)
-3
-4
-5
-6
1
0
-1
(b)
P
DSR
ET
P (mm mo^{-1}) / DSR (W m^{-2})
ET (mm mo^{-1})
350
200
50
150
125
100
(c)
P
ET
P (mm yr^{-1})
ET (mm yr^{-1})
2660
2460
2220
1410
1380
2003
2005
2007
2009
2011
2013

Figure 11.

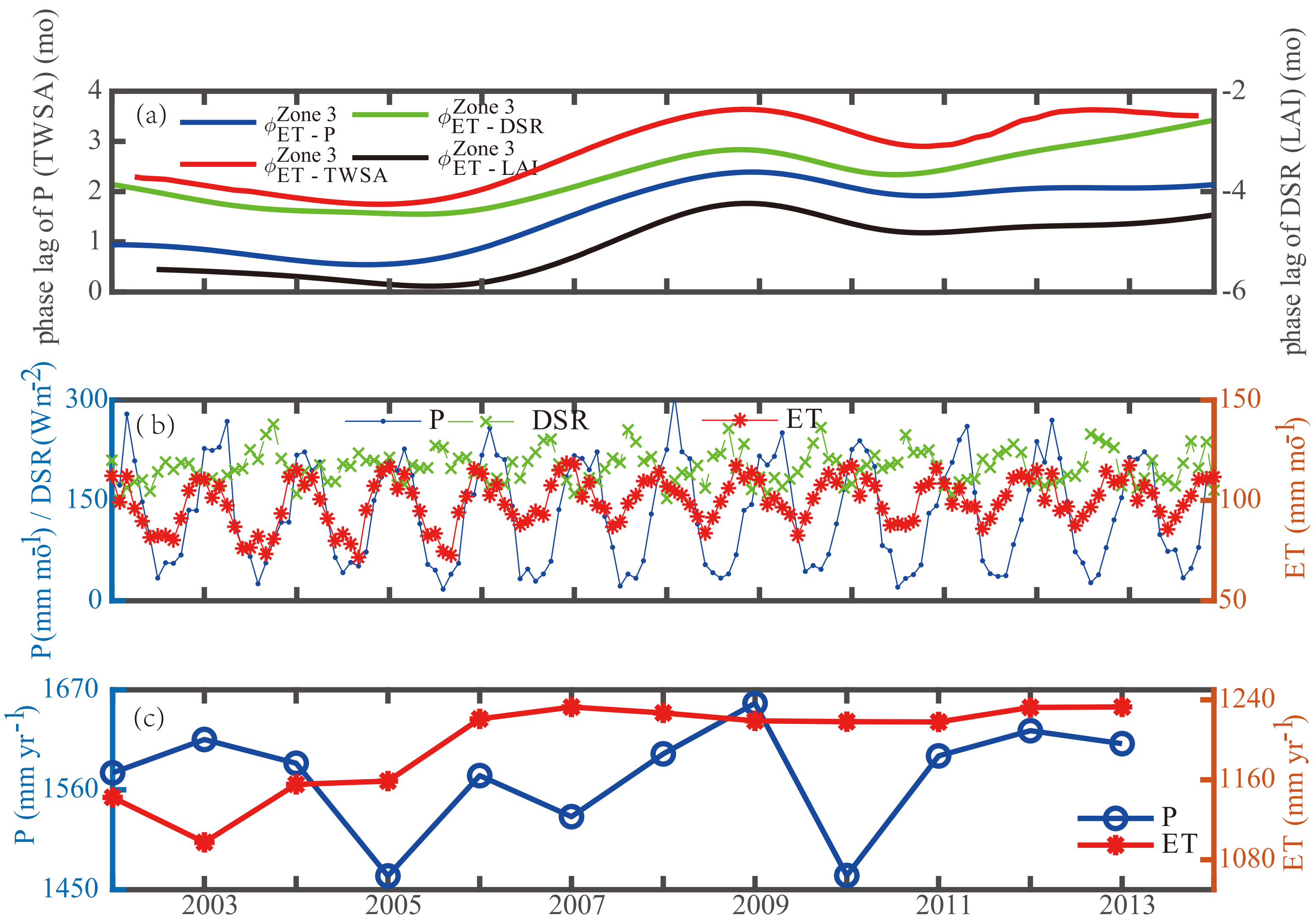

(a)
$\phi^{Zone\ 3}_{ET\ -\ P}$
$\phi^{Zone\ 3}_{ET\ -\ DSR}$
$\phi^{Zone\ 3}_{ET\ -\ TWSA}$
$\phi^{Zone\ 3}_{ET\ -\ LAI}$
phase lag of P (TWSA) (mo)
phase lag of DSR (LAI) (mo)
(b)
P
DSR
ET
P(mm mo-1) / DSR(W m-2)
ET (mm mo-1)
(c)
P
ET
P (mm yr-1)
ET (mm yr-1)
2003
2005
2007
2009
2011
2013

Figure 12.

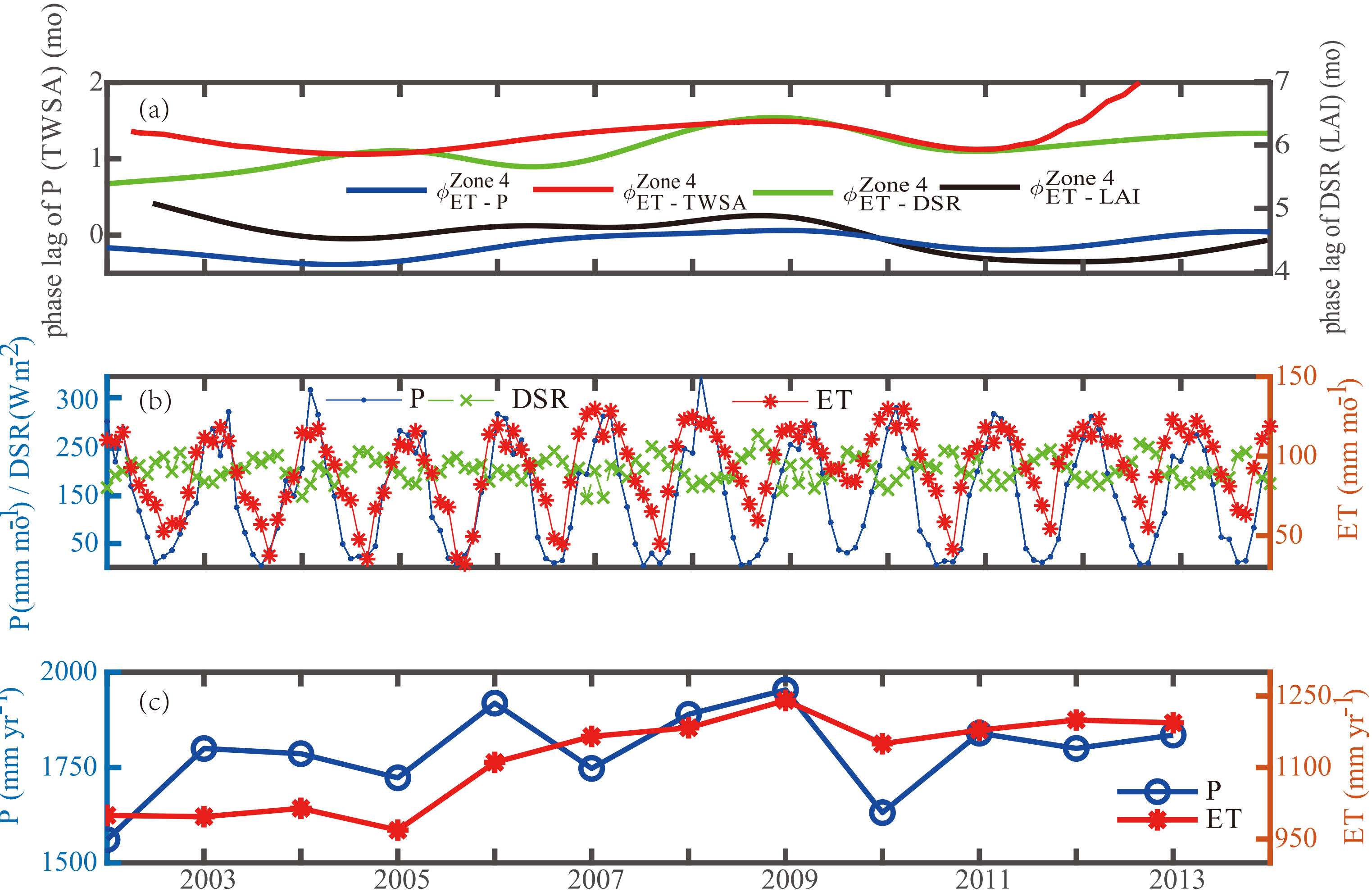

(a)
(b)
(c)
phase lag of P (TWSA) (mo)
phase lag of DSR (LAI) (mo)
$\phi^{Zone\ 4}_{ET - P}$
$\phi^{Zone\ 4}_{ET - TWSA}$
$\phi^{Zone\ 4}_{ET - DSR}$
$\phi^{Zone\ 4}_{ET - LAI}$
P
DSR
ET
P(mm mo^{-1}) / DSR(W m^{-2})
ET (mm mo^{-1})
P (mm yr^{-1})
ET (mm yr^{-1})
2003
2005
2007
2009
2011
2013